



Relativistic effects on the kink of nuclear charge radii in lead

Saturnino Marcos^{1,a}, Ramón Niembro^{1,b}, Mercedes López-Quelle^{2,c}

¹ Departamento de Física Moderna, Universidad de Cantabria, 39005 Santander, Spain

² Departamento de Física Aplicada, Universidad de Cantabria, 39005 Santander, Spain

Received: 12 February 2024 / Accepted: 17 March 2024 / Published online: 29 March 2024

© The Author(s) 2024

Communicated by Dario Vretenar

Abstract The kink in the nuclear charge radii of lead isotopes is studied in the relativistic mean field approximation framework, using the parameter set NL3*. Within this approach, it is shown that the small component of the single-particle Dirac spinors plays an essential role in the kink formation through its effects on the single-particle central potential. This is because the structure of this potential in terms of the σ -scalar and ω -vector fields and the contributions of the small component to the scalar and nucleon densities have opposite signs. The impact of the spin-orbit interaction of the valence neutrons on the kink, through its effects on their wave functions, is very small for $1i$ states but significant for $2g$ states. Due to relativistic contributions, the effects on the kink of neutrons in the valence levels of a spin-orbit doublet with $j = l + 1/2$ and $j = l - 1/2$ are rather different from each other, even in the limit case of neglecting their spin-orbit interaction.

1 Introduction

The nuclear root-mean-square (rms) charge radius is one of the most important macroscopic magnitudes of atomic nuclei. In an appropriate nuclear model, it depends on the nucleon-nucleon interaction, the equation of state of nuclear matter and the characteristics of the model. Consequently, for confidence in the model's reliability, a reasonable prediction of this magnitude is required. Traditionally, the rms has been measured through electron scattering. Currently, laser spectroscopy makes it possible to measure slight differences between the radii of two members of an isotopic family with a high degree of precision [1], which is impossible via electron scattering. This fact increases the relevance of the

mean-square charge radii (r_c^2) differences within an isotopic family.

For many years, it has been recognised that in certain isotopic chains, a pronounced shift in the behaviour of the nuclear charge radii occurs as the number of neutrons crosses a specific value. The most typical example of this abrupt change occurs in the charge radii of Pb isotopes [2]. It appears when the neutron number (N) becomes greater than $N = 126$ and is generally known as kink or kink effect (KE). This kink is faithfully replicated by the nuclear relativistic mean-field approximation (RMFA) [2–7], while non-relativistic Skyrme-Hartree-Fock (SHF) models with standard parametrisations fail to reproduce it [8]. Nevertheless, the RMFA have problems reproducing the kink in the Sn family at $N = 82$ [7,9].

The reason why the relativistic and non-relativistic mean-field models provide different results for the kink has been discussed in several studies. Thus, in Ref. [10], it is contended that the inability of standard Skyrme interactions to account for the kink is attributed to the somewhat large spin-orbit interaction resulting from the isospin dependence of the Skyrme functionals. In the family of Pb isotopes, the spin-orbit interaction influences the relative positioning of the neutron $2g_{9/2}$ and $1i_{11/2}$ energy levels. This indirectly affects the occupancy of these levels and significantly determines the proton density for $N > 126$. While in typical SHF functionals, the energy of the $2g_{9/2}$ level usually falls significantly below that of the $1i_{11/2}$ level (in qualitative agreement with experimental data), in relativistic models, these two levels are either close to or in reversed order. It is accepted that this inverted order promotes the emergence of the kink, as a higher occupancy of the $1i_{11/2}$ orbital compared to the $2g_{9/2}$ orbital favours an expansion of the charge radii [3,6,11,12]. (For simplicity, we often refer to the subshells nl_j as orbitals). Thus, new Skyrme functionals have been developed [10,13] by modifying the relation between the spin-orbit strengths of

^a e-mail: marcoss@unican.es (corresponding author)

^b e-mail: niembror@unican.es

^c e-mail: lopezqm@unican.es

the isovector part (W'_0) and the isoscalar part (W_0) to approach that of the RMFA.

A different method proposed by Fayans et al. [14–17], in the context of non-relativistic mean-field functionals, involves introducing density gradient dependence into the surface and pairing terms. After adjusting the parameters, this method allows a simultaneous description of odd-even staggering effects in energies and charge radii. However, the microscopic origin of these terms has been questioned [6]. Influenced by the chiral effective field theory, an alternative approach incorporated a density-dependent component associated with three-nucleon forces in the spin-orbit interaction [9, 12, 18]. These methods have helped to increase the magnitude of the kink in the charge radii of lead isotopes, bringing it closer to the experimental value. Yet, in references [7, 11], a reasonable kink was achieved while sticking with $W'_0 = W_0$, like in standard Skyrme functionals, as long as the value of W_0 is set correctly to ensure a high probability of occupying the neutron $1i_{11/2}$ level.

Several research groups have recently reported substantial advances in understanding the mechanism responsible for the kink effect. For example, the effect of the core swelling due to the pairing interaction that, globally, reduces the radius of valence neutron orbitals is discussed in Ref. [19]. The effects of the tensor interaction in relativistic models through its impact on the spin-orbit potential, which influences the occupancy probabilities of sp neutron states, and symmetry energy are considered important in Ref. [7]. However, for a given neutron configuration, the global effects of tensor interactions are small, as noted in [20]. In Refs. [21, 22], in addition to the symmetry energy, the particle-vibration coupling in A odd nuclei is also considered relevant. In the present work, we will consider only even-even nuclei. In Refs. [11, 23], the crucial role played by the neutron orbital $1i_{11/2}$ in the kink is related to its large overlap with the nodeless proton orbitals that contribute the most to the kink [4, 11]. However, this conclusion is based on the hypothesis that these overlaps give a measure of the interaction between neutrons and protons in these orbitals, which is not justified. A detailed review of the effort made to understand the behaviour of the charge radii in different isotopic families is given in Ref. [6].

This work investigates the mechanism that determines the kink formation within the RMFA in the lead isotopic family. We examine, in particular, how the neutron orbitals $1i$ and $2g$ intervene in the mechanism and how it is modified in the non-relativistic limit. Our analyses focus on two key aspects: firstly, the impact of the spin-orbit interaction on the charge radius through its influence on the single-particle (sp) wave functions, and secondly, the effect of valence neutrons on the charge radius via their influence on the effective sp central potential.

The paper is organised as follows. In Sect. 2, we provide brief descriptions of the relativistic model and the

Schrödinger-like equation equivalent to the Dirac equation used in the calculations. The results for the nuclear charge radius in lead isotopes are discussed in Sect. 3. We analyse the impact of the spin-orbit interaction on the charge radius through its influence on the sp wave functions of the valence neutrons in Sect. 3.1. The role of the small component of the sp Dirac spinors of the valence neutrons in the mechanism that explains the generation of the kink is provided in Sect. 3.2. We analyse how the density distributions of proton orbitals respond to the perturbation in the central potential of the Schrödinger-like equation caused by the valence neutrons. The conclusions are given in Sect. 4.

2 The relativistic model

In the calculations, we use the RMFA [24–28] with the parameter set NL3* [28] as an appropriate example of a relativistic model. We assume the no-see (or tree) approximation, that is, the nuclear ground state contains nucleons only in sp states of positive energy. In other words, the possibility of the creation and annihilation of pairs nucleon-antinucleon by the nucleon field is not considered [29–31]. The time-independent Dirac spinor $\psi_a(\vec{r})$ for a nucleon with the rest mass M in the state a satisfies the time-independent Dirac equation [25, 27]

$$\{-i\hbar\vec{\alpha} \cdot \vec{\nabla} + \beta[M + S(\vec{r})] + V(\vec{r})\}\psi_a(\vec{r}) = E_a\psi_a(\vec{r}), \quad (1)$$

where $E_a = M + \epsilon_a$, $-\epsilon_a$ is the binding energy corresponding to the state $\psi_a(\vec{r})$. $S(\vec{r})$ and $V(\vec{r})$ are the so-called scalar and vector sp potentials generated through the exchange between nucleons of the scalar (σ) and vector (ω , ρ , γ) bosons, respectively. They are defined as

$$S(\vec{r}) = g_\sigma \sigma(\vec{r}), \quad (2)$$

$$V(\vec{r}) = g_\omega \omega_0(\vec{r}) + \tau_3 g_\rho \rho_{0,3}(\vec{r}) + \frac{1 + \tau_3}{2} V_C(\vec{r}), \quad (3)$$

where, $\sigma(\vec{r})$ is the static scalar mean field associated to the σ -meson (effective particle to describe the exchange of two-pion, coupled to zero angular momentum, between nucleons), $\omega_0(\vec{r})$ and $\rho_{0,3}(\vec{r})$ are the time components (surviving in the RMFA) of the ω_μ and $\vec{\rho}_\mu$ static mean fields associated to the ω - and ρ -mesons, respectively, while V_C is the Coulomb potential. The arrow in the $\vec{\rho}_\mu$ field indicates that it is a vector in the isospin space. The quantities g_σ , g_ω and g_ρ are the coupling constants associated with the interaction of the σ -, ω - and ρ -meson fields, respectively, and the nucleon field. $\tau_3 = 1$ for a proton state and $\tau_3 = -1$ for a neutron state.

The effective density Lagrangian corresponding to the NL3* set contains a potential energy that includes cubic and quartic self-interacting terms in the scalar field [24, 28]: $\frac{1}{3}b\sigma^3(\vec{r}) + \frac{1}{4}c\sigma^4(\vec{r})$, where b and c are parameters fitted in

the model. The static meson field equations can be written in the form [25–27]:

$$[-\vec{\nabla}^2 + m_\sigma^{*2}(\vec{r})]\sigma(\vec{r}) = -g_\sigma \rho_S(\vec{r}), \tag{4}$$

$$[-\vec{\nabla}^2 + m_\omega^2]\omega_0(\vec{r}) = g_\omega \rho_B(\vec{r}), \tag{5}$$

$$[-\vec{\nabla}^2 + m_\rho^2]\rho_{0,3}(\vec{r}) = g_\rho \rho_3(\vec{r}), \tag{6}$$

where

$$m_\sigma^{*2}(\vec{r}) = m_\sigma^2 + b\sigma(\vec{r}) + c\sigma^2(\vec{r}) \tag{7}$$

and m_σ , m_ω and m_ρ are the σ -, ω - and ρ -meson masses, respectively. $\rho_S(\vec{r})$ is the scalar density, $\rho_B(\vec{r})$ is the usual (nucleon, baryon or vector) density. $\rho_3(\vec{r})$ is the isovector density: difference between the proton $\rho_p(\vec{r})$ and neutron $\rho_n(\vec{r})$ densities.

For nuclei with spherical symmetry, that we will assume in this work, all densities, fields and potentials also have spherical symmetry: $\rho_{n,p}(\vec{r}) \rightarrow \rho_{n,p}(r)$, $\rho_S(\vec{r}) \rightarrow \rho_S(r)$, $\rho_B(\vec{r}) \rightarrow \rho_B(r)$, $\rho_3(\vec{r}) \rightarrow \rho_3(r)$, $\sigma(\vec{r}) \rightarrow \sigma(r)$, $\omega_0(\vec{r}) \rightarrow \omega_0(r)$, $\rho_{0,3}(\vec{r}) \rightarrow \rho_{0,3}(r)$, $V_C(\vec{r}) \rightarrow V_C(r)$, $S(\vec{r}) \rightarrow S(r)$ and $V(\vec{r}) \rightarrow V(r)$.

In the standard notation, $\psi_a(\vec{r})$ can be written as

$$\psi_a(\vec{r}) = \begin{bmatrix} \phi_a(\vec{r}) \\ \zeta_a(\vec{r}) \end{bmatrix} = \frac{1}{r} \begin{bmatrix} iG_a(r) \\ F_a(r)\vec{\sigma} \cdot \hat{\mathbf{r}} \end{bmatrix} y_{j_a l_a}^{m_a}(\hat{\mathbf{r}}) \chi_{\frac{1}{2}}^a, \tag{8}$$

where $\frac{G_a(r)}{r}$ and $\frac{F_a(r)}{r}$ represent the radial part of the large and small components, respectively, $y_{j_a l_a}^{m_a}(\hat{\mathbf{r}})$ stands for a normalized spin-angular function and $\chi_{\frac{1}{2}}^a$ is the nucleon isospinor [29,32].

In spherical finite nuclei, the neutron $\rho_n(r)$ and proton $\rho_p(r)$ densities and the scalar density $\rho_S(r)$ can be written as

$$\rho_{n,p}(r) = \sum_{a \in occ} \frac{2j_a + 1}{4\pi} \frac{G_a^2(r) + F_a^2(r)}{r^2}, \tag{9}$$

where a represents an occupied state of neutron for $\rho_n(r)$ and proton for $\rho_p(r)$;

$$\rho_S(r) = \sum_{a \in occ} \frac{2j_a + 1}{4\pi} \frac{G_a^2(r) - F_a^2(r)}{r^2}, \tag{10}$$

where a represents an occupied neutron or proton state. The densities $\rho_B(r)$ and $\rho_3(r)$ can be written in terms of $\rho_n(r)$ and $\rho_p(r)$, as

$$\rho_B(r) = \rho_n(r) + \rho_p(r), \tag{11}$$

$$\rho_3(r) = \rho_p(r) - \rho_n(r). \tag{12}$$

2.1 The Schrödinger-like equation equivalent to the Dirac equation

To facilitate the comparison of the predictions of the relativistic and non-relativistic mean-field models on the kink effect, we construct a Schrödinger-like equation equivalent to the Dirac equation. This can be achieved from Eq. (1)

by writing the small component $\zeta_a(\vec{r})$ of the Dirac spinors in terms of the large component $\phi_a(\vec{r})$, and considering the transformation [33]

$$\phi(\vec{r}) = B(r)^{1/2} \tilde{\phi}(\vec{r}), \tag{13}$$

where the subscript a is removed for simplicity, and

$$B(r) \equiv 2M + \epsilon + S(r) - V(r). \tag{14}$$

Then, in terms of $\tilde{\phi}(\vec{r})$, the Schrödinger-like equation can be written as

$$\left[-\frac{\hbar^2}{2M} \nabla^2 + V_{\text{cent}}(r, \epsilon) + V_{\text{SO}}(r, \epsilon) \right] \tilde{\phi}(\vec{r}) = \epsilon \tilde{\phi}(\vec{r}), \tag{15}$$

where the central ($V_{\text{cent}}(r, \epsilon)$) and the spin-orbit ($V_{\text{SO}}(r, \epsilon)$) potentials are energy dependent [3,33]. They read as follows:

$$V_{\text{cent}}(r, \epsilon) = S + V + \frac{S^2 - V^2 + \epsilon^2}{2M} + \epsilon \frac{V}{M} + \delta V_{\text{cent}}(r, \epsilon), \tag{16}$$

$$\delta V_{\text{cent}}(r, \epsilon) = \frac{\hbar^2}{2M} \left[\frac{1}{4} W^2 + \frac{1}{r} W + \frac{1}{2} W' \right],$$

$$W(r, \epsilon) = -\frac{S' - V'}{2M + \epsilon + S - V};$$

$$V_{\text{SO}}(r, \epsilon) = \frac{\hbar^2}{2M} \frac{2}{r} W(r, \epsilon) \vec{l} \cdot \vec{s}. \tag{17}$$

Writing the radial part of $\tilde{\phi}(\vec{r})$ as $g(r)/r$, we get from Eq. (13)

$$G(r) = B(r)^{1/2} g(r). \tag{18}$$

From Eq. (15), it can be obtained for $g(r)$ the following Schrödinger-like equation [30]:

$$-\frac{\hbar^2}{2M} g''(r) + V_{\text{eff}}(r, \epsilon) g(r) = \epsilon g(r), \tag{19}$$

where (in the standard notation)

$$V_{\text{eff}}(r, \epsilon) = V_{\text{cent}}(r, \epsilon) + \frac{\hbar^2}{2M} \frac{l(l+1)}{r^2} + V_{\text{SO}}(r, \epsilon). \tag{20}$$

The small component $F(r)$ of a Dirac spinor can be obtained from their corresponding large component $G(r)$ through the equation [30,32]

$$F(r) = \frac{\hbar[G'(r) + (k/r)G(r)]}{B(r)}, \tag{21}$$

where $k = j + 1/2$ for the states with $j = j_- \equiv l - 1/2$ and $k = -(j + 1/2)$ for states with $j = j_+ \equiv l + 1/2$. The normalization condition for $G(r)$ and $F(r)$ reads

$$\int [G^2(r) + F^2(r)] dr = 1. \tag{22}$$

The functions $G(r)$ and $F(r)$ obtained in the way described above satisfy the Dirac Eq. (1). However, if $F(r)$ is neglected

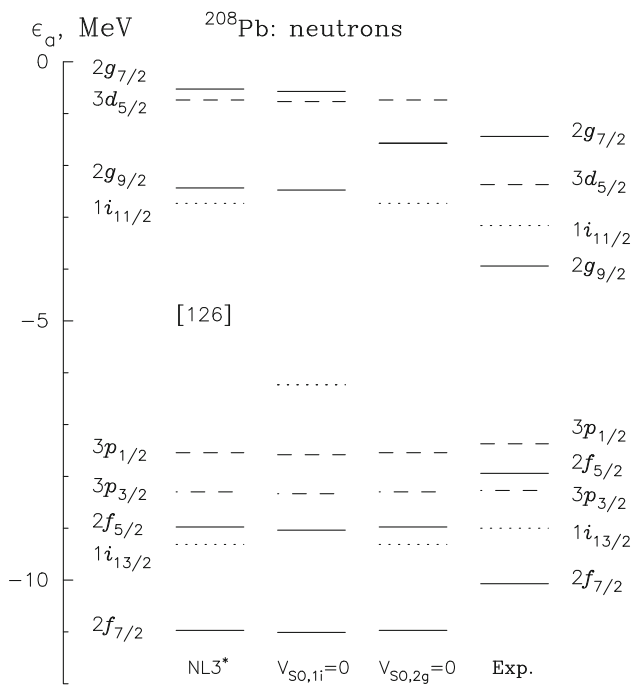


Fig. 1 Single-neutron energies of the ^{208}Pb nucleus calculated in the RMFA with the NL3* parameter set. We use the complete model (label NL3*) and take $V_{\text{SO}}(r, \epsilon) = 0$ in Eq. (15), alternatively, for the $1i$ states (label $V_{\text{SO},1i} = 0$), being the $1i_{13/2}$ level full and the $1i_{11/2}$ level empty, and for the empty $2g$ states (label $V_{\text{SO},2g} = 0$). The experimental values shown in the column labelled Exp. are taken from Ref. [34]

in Eq. (22), Eqs. (15–20, 22) represent a non-relativistic approximation to Eq. (1).

3 Results

The magnitude of the kink in the lead isotopes has been related to the positions of the neutron energy levels $1i_{11/2}$ and $2g_{9/2}$ [3, 4, 7, 9–11], which depend on the spin-orbit (SO) interaction. Figure 1 shows the neutron levels of the ^{208}Pb nucleus calculated in the RMFA with the NL3* parameter set. The column labelled NL3* corresponds to the results of the standard calculation (complete model). In contrast, the columns labelled $V_{\text{SO},1i} = 0$ and $V_{\text{SO},2g} = 0$ correspond to the results obtained when the SO interaction has been suppressed by hand in Eqs. (15) and (20) (throughout the calculation) for the partially empty $1i$ and completely empty $2g$ neutron levels, respectively (see figure caption). In what follows, the $1i$ and $2g$ orbitals will refer always to neutrons (ν).

The charge radius isotope shift for the lead isotopic family relative to the ^{208}Pb nucleus is defined as

$$\Delta\langle r_c^2 \rangle = r_c^2(^A\text{Pb}) - r_c^2(^{208}\text{Pb}). \quad (23)$$

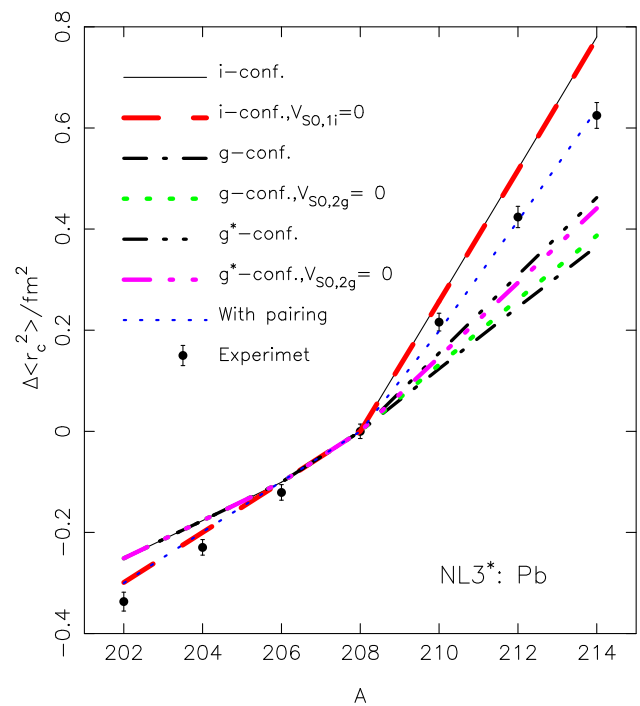


Fig. 2 The nuclear charge radius isotope shift $\Delta\langle r_c^2 \rangle$ of the ^APb isotopes relative to the ^{208}Pb nucleus, calculated in the RMFA with the parameter set NL3*, is plotted for several cases: the “ i -conf.,” “ g -conf.” and “ g^* -conf.” as indicated in Sect. 3, and including pairing correlations for neutrons in the BCS approximation [35]. We used the three-point odd-even staggering formula for the energy gaps. The “ $V_{\text{SO},1i} = 0$ ” and “ $V_{\text{SO},2g} = 0$ ” labels indicate that $V_{\text{SO}}(r, \epsilon) = 0$ was taken for the $1i$ - and $2g$ -neutron states, respectively. The points with the error bars correspond to the experimental values taken from Ref. [36]. For simplicity, we avoid drawing the values corresponding to A integer with special marks

The corresponding results in the RMFA with the NL3* set are shown in Fig. 2 for three configurations with SO interaction (complete model) and without SO interaction for the $\nu 1i$ and $\nu 2g$ orbitals, and the complete model including neutron pairing correlations (see figure caption).

For the complete model, it can be seen that the kink is somewhat overestimated for the $[^{208}\text{Pb}](1i_{11/2})^{N-126}$ configuration (i -conf.), i.e., when the valence neutrons for the lead isotopes with $N > 126$ occupy the $1i_{11/2}$ level. However, the kink practically disappears for the $[^{208}\text{Pb}](2g_{9/2})^{N-126}$ configuration (g -conf.), as also found in [6]. (For simplicity, “-conf.” will be written simply as “-conf”). This behaviour of the kink for the i -conf and g -conf is also exhibited in the RMFA for older parameter sets as, for example, NL-SH, NL3 [3] or NL-Z [26], and some SHF functionals [11].

In our model, the energies of the neutron orbitals $1i_{11/2}$ and $2g_{9/2}$ in lead isotopes for $A \sim 208$ are close to each other. Therefore, one can expect that, by including neutron pairing correlations, the magnitude of the kink will come closer to the experimental value. This is confirmed in Ref.

[6] using the relativistic Hartree-Bogoliubov method or by our results shown in Fig. 2, using the simple BCS approximation [35]. This is what happens too, for example, in the RMFA with the NL-Z set [10] or in the relativistic Hartree-Fock Approximation for appropriate parametrisations [4] (results for other relativistic models can be found in [6]). In this work, the results with pairing correlations are not discussed in detail because we are focused on understanding the mechanism by which the states $1i$ and $2g$ intervene in the kink formation.

The g^* -conf label in Fig. 2 corresponds to the results of placing $N - 126$ neutrons in the $2g_{7/2}$ states (with $j = j_-$, $E_{2g_{7/2}} \simeq -1.0$ MeV for ^{214}Pb), instead of in the $2g_{9/2}$ ones (with $j = j_+$) as for the g -conf. The magnitude of the kink has increased sensibly with respect to that of the g -conf. We take into account that for the ^{214}Pb nucleus, the rms neutron radius $\langle r_{2g_{7/2}} \rangle \simeq 7.33$ fm is slightly larger than $\langle r_{2g_{9/2}} \rangle \simeq 7.08$ fm. With this result, it cannot be ruled out the possibility that the greater magnitude of the kink for the g^* -conf than for the g -conf may be due, in part, to the fact that $\langle r_{2g_{7/2}} \rangle > \langle r_{2g_{9/2}} \rangle$. Notice that in Ref. [10], a greater ability to increase the nuclear charge radius is attributed to the neutrons in the $1i_{11/2}$ or $2g_{9/2}$ orbitals as their rms radii increase.

3.1 The spin-orbit interaction for the valence neutron orbitals and the kink effect

As mentioned above, it is known that the SO interaction strongly affects the kink indirectly by influencing the sp energies of the valence neutrons, which, in turn, determine their occupancy probabilities [7, 9–11, 13].

To analyse a possible direct effect of this interaction, we neglect the $V_{\text{SO}}(r, \epsilon)$ potential in Eqs. (19, 20), alternatively, for the $1i$ and $2g$ states throughout the calculation. The corresponding neutron sp levels for ^{208}Pb are shown in the columns labelled as $V_{\text{SO},1i} = 0$ and $V_{\text{SO},2g} = 0$, respectively, in Fig. 1. For the case $V_{\text{SO},1i}(r, \epsilon) = 0$, the degenerate levels $1i_{13/2}$ and $1i_{11/2}$ will be the least bound levels occupied by neutrons. If 14 neutrons are placed in the $1i_{13/2}$ orbital, the same configuration as that of the complete relativistic model in the ground state is obtained. Then, if for $A > 208$, neutrons are added to the $1i_{11/2}$ orbital, a kink almost identical to that of the complete model with the i -conf is formed, as can be seen in Fig. 2, line “ i -conf., $V_{\text{SO},1i} = 0$ ”. The two lines, with and without SO interaction for the $1i$ states in the i -conf, practically coincide for $A > 208$; The slight differences observed for $A < 208$ can be attributed to the distinct filling orders of the sp energy levels in the two lines. We also notice that, quite generally, $\langle r_{1i_{11/2}} \rangle \simeq \langle r_{1i_{13/2}} \rangle$ (see below).

The above results show that, even without SO interaction for the $1i$ -states, the i -conf of the lead family is as kinky as it is when the SO interaction is present. From the point of view of a non-relativistic mean-field formalism, this is unexpected. In fact, in the non-relativistic limit of the RMFA considered

in this work, i.e., neglecting the small component of the $1i$ Dirac spinors in Eq. (22), the result obtained for the “ i -conf., $V_{\text{SO},1i} = 0$ ” case is not possible. From Eqs. (19) and (20), it can be seen that taking $V_{\text{SO}}(r, \epsilon) = 0$, the states belonging to a SO doublet are degenerate, and their corresponding $g(r)$ functions (and consequently also the $G(r)$ ones) satisfy the same linear equation. Then, they must be proportional to each other. As explained above, in the non-relativistic limit, the small component of the sp Dirac spinors is neglected in Eq. (22). Then, the $g(r)$ and $G(r)$ functions of the two SO partners will be identical. Consequently, if $V_{\text{SO},1i}(r, \epsilon) = 0$, not kink effect (KE) is possible for the lead isotopic family in the i -conf.

However, in the relativistic formalism, when the small components of the Dirac spinors are considered, the situation is different. The functions $F_{j=j_+}(r)$ and $F_{j=j_-}(r)$ for the states of a SO doublet are different, even in the hypothetical case that $V_{\text{SO}}(r, \epsilon) = 0$, as can be seen from Eq. (21). Consequently, the normalization condition for the sp Dirac spinors given by Eq. (22) implies that the corresponding $G_{j=j_+}(r)$ and $G_{j=j_-}(r)$ functions of the SO doublet cannot be identical but only proportional to each other. Thus, in the relativistic models, even if $V_{\text{SO}}(r, \epsilon) = 0$, the radial parts of the two components of the sp Dirac spinors of a SO doublet are different, in contrast to what happens in the non-relativistic mean-field formalism. This is because the Dirac spinors obey a Dirac equation rather than a Schrödinger equation.

The kink obtained in the relativistic “ i -conf., $V_{\text{SO},1i} = 0$ ” case is because the radial parts of the small components of the $1i_{13/2}$ and $1i_{11/2}$ orbitals are different from each other. Thus, an abrupt change in the trend of the magnitude of the charge radius appears when A increases from $A = 208$ to $A = 210$ (being filling the $1i_{11/2}$ level). We remark that $\langle r_{1i_{11/2}} \rangle \lesssim \langle r_{1i_{13/2}} \rangle$ for $^{208-214}\text{Pb}$, i.e., the radius of the neutron orbital responsible for the kink in this isotopic family is smaller than that of its SO partner, which rules out the possibility that the KE could be attributed to the fact that $\langle r_{1i_{11/2}} \rangle$ be larger than $\langle r_{1i_{13/2}} \rangle$. This result indicates that factors other than the magnitudes of $\langle r_{1i_{11/2}} \rangle$ and $\langle r_{1i_{13/2}} \rangle$ are involved in the formation of the kink. For the i -conf (with $V_{\text{SO},1i}(r) \neq 0$), we will see in subsection 3.2 that, ultimately, the small component of the $\nu 1i_{11/2}$ orbital is also primarily responsible for the KE.

In the “ i -conf., $V_{\text{SO},1i} = 0$ ” case that we are studying, the $1i$ states are degenerate. Thus, we can consider filling the $1i_{11/2}$ level before the $1i_{13/2}$ one for the lead isotopes with $195 \leq A \leq 206$. Then, as A increases, an anti-kink (or kink inverted) is found at $A = 206$ due to the change of the charge radius slope as the $1i_{13/2}$ level is filling. Actually, as the $1i_{13/2}$ and $1i_{11/2}$ orbitals are degenerate, for $A \geq 195$, neutrons would try to share these two orbitals and one can imagine a strong cancellation between the kink at $A = 208$

and the anti-kink at $A = 206$. Then, if the SO interaction were re-established for the $1i$ -states, the normal ordering of energy levels for the $1i$ -states would be recovered and the normal kink would show up even if the wave function were not modified by the SO interaction (because, according to the results of Fig. 2, for $V_{\text{SO},1i}(r) = 0$ and $V_{\text{SO},1i}(r) \neq 0$ the kinks are very similar). However, this behaviour cannot be reproduced by the non-relativistic mean-field models. This is because, in these models, to generate a kink when neutrons are filling the $1i_{13/2}$ and $1i_{11/2}$ orbitals, the wave functions of the two SO partners should be modified significantly by the SO interaction.

The results outlined in this Subsection show that when $V_{\text{SO},1i}(r) = 0$ and neutrons are added to the lead $1i_{11/2}$ orbital for $N > 126$, the relativistic models will exhibit a more rapid increase in the nuclear charge radius than the non-relativistic mean-field models. Thus, as the strength of the SO interaction is recovered from zero to its typical value, the former models will start with a larger kink than the latter. This indicates that a larger kink can generally be expected for relativistic models than for non-relativistic ones, as noted in [7].

Now, we consider a case identical to the g -conf previously discussed but with $V_{\text{SO},2g}(r) = 0$ throughout the calculation. The corresponding results are labelled as “ g -conf., $V_{\text{SO},2g} = 0$ ” in Fig. 2. They show a slight *increase* in the magnitude of the kink relative to that of the complete model ($V_{\text{SO},2g} \neq 0$). We notice that for ^{214}Pb , $\langle r_{2g_{9/2}, V_{\text{SO},2g}=0} \rangle \simeq 7.22$ fm, which is slightly greater than $\langle r_{2g_{9/2}, V_{\text{SO},2g} \neq 0} \rangle \simeq 7.08$ fm.

Finally, the case labelled as “ g^* -conf., $V_{\text{SO},2g} = 0$ ” in Fig. 2 is identical to the case labelled as “ g^* -conf.”, but with $V_{\text{SO},2g}(r) = 0$ throughout the calculation. A slight *decrease* in the magnitude of the kink can be observed compared to that of the corresponding complete model ($V_{\text{SO},2g} \neq 0$). For ^{214}Pb , $\langle r_{2g_{7/2}, V_{\text{SO},2g}=0} \rangle \simeq 7.24$ fm, which is slightly smaller than $\langle r_{2g_{7/2}, V_{\text{SO},2g} \neq 0} \rangle \simeq 7.33$ fm.

The results of the two previous paragraphs indicate that the effect of the SO interaction on the $2g_{9/2}$ and $2g_{7/2}$ orbitals has a small influence of opposite sign on the magnitude of their corresponding kinks. This influence may be attributed, in part, to the tiny effects of the SO interaction on the neutron rms radii of the $2g$ orbitals, as an increase (decrease) in the magnitude of the kink with the SO interaction aligns with an increase (decrease) in the neutron rms radius of the $2g_{9/2}$ or $2g_{7/2}$ orbitals.

However, if we compare the results for the two cases with $V_{\text{SO},2g} = 0$ considered, we can see that the magnitude of the kink is appreciably larger for the “ g^* -conf., $V_{\text{SO},2g} = 0$ ” (with $j_{2g_{7/2}} = j_-$) than for the “ g -conf., $V_{\text{SO},2g} = 0$ ” (with $j_{2g_{9/2}} = j_+$), although now $\langle r_{2g_{7/2}} \rangle = 7.24$ fm \simeq $\langle r_{2g_{9/2}} \rangle = 7.22$ fm. The different magnitude of the kink in these two cases must be attributed to relativistic effects that

make the wave functions of the two SO partners $2g_{7/2}$ and $2g_{9/2}$ different from each other.

From the results depicted in Fig. 2 and discussed earlier in this subsection, it is clear that for the lead isotopic family, neutrons from the $1i$ and $2g$ SO doublets in states with $j = j_-$ are more efficient than in states with $j = j_+$ in increasing the magnitude of the kink (without this being attributable to their different rms radii). Thus, concerning the KE, the behaviour of the $1i_{11/2}$ and $1i_{13/2}$ orbitals is notably different, more than that of the $2g_{7/2}$ and $2g_{9/2}$ orbitals. In the case of neglecting the SO interaction for orbitals $1i$ and $2g$, we will see in Subsec. 3.2 that $G_{j_-}(r)$ and $G_{j_+}(r)$ are almost identical for the two SO partners. Consequently, the different behaviour of the orbitals of two SO partners arises almost entirely from differences in the small components.

In the realistic case of considering the SO interaction, it turns out that for two SO partners, $G_{j_-}(r) \simeq G_{j_+}(r)$, while $F_{j_-}(r)$ and $F_{j_+}(r)$ are rather different (roughly, as in the case of neglecting the SO interaction). As the $F(r)$ functions are quite small, an accurate numerical calculation is necessary to show the effect of the differences $F_{j_-}(r) \neq F_{j_+}(r)$ and $G_{j_-}(r) \neq G_{j_+}(r)$ on the nuclear rms charge radius.

3.2 Small component of the Dirac spinors and the kink effect

In the previous Subsection, we have found indications that, in the RMFA, the kink in lead isotopes is significantly influenced by the contribution of the small component of the sp Dirac spinors of valence neutrons on the scalar and nucleon density distributions. In this subsection, we will delve into this topic for the i -conf, g -conf, and g^* -conf defined above. To do this, we solve Eq. (19) to obtain $g(r)$ and determine $G_a(r)$ using Eq. (18) for all occupied sp states. Then, in the configuration considered, we set the corresponding $F_{1i_{11/2}}(r)$, $F_{2g_{9/2}}(r)$, or $F_{2g_{7/2}}(r)$ function equal to zero. The remaining $F_a(r)$ functions of the occupied orbitals are calculated from Eq. (21). All the sp Dirac spinors are normalised to unity according to Eq. (22).

The results for the charge radius isotope shift $\Delta \langle r_c^2 \rangle$ are shown in Fig. 3. For the three configurations considered, it is observed that the magnitude of the kink strongly decreases by a similar amount when the small component of the neutron orbital characterising the configuration is neglected. (In fact, for the g -conf and g^* -conf, the orientation of the kink in the figure becomes inverted to the normal one, i.e. it becomes an anti-kink). The different magnitudes of the kink corresponding to the cases “ g -conf., $F(2g_{9/2}) = 0$ ” and “ g^* -conf., $F(2g_{7/2}) = 0$ ” in Fig. 3 are due, essentially, to the SO interaction, which is mainly responsible for $G_{2g_{9/2}} \neq G_{2g_{7/2}}$ (because the potential $V_{\text{cent}}(r, \epsilon)$ in Eq. (15) is very similar for both orbitals, owing to its relatively small energy dependence). This conclusion is consistent with the result of Fig. 2,

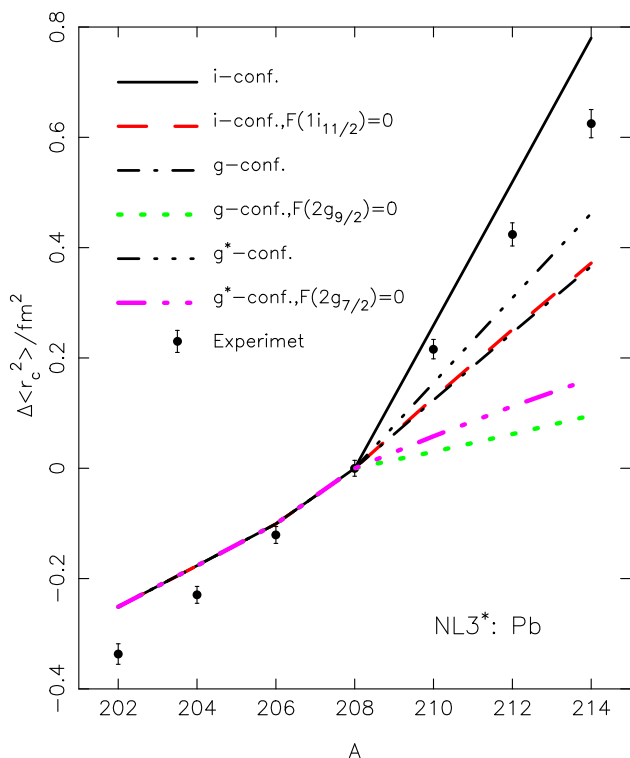


Fig. 3 The nuclear charge radius isotope shift $\Delta\langle r_c^2 \rangle$ of the ^APb isotopes relative to the ^{208}Pb nucleus in the RMFA with the parameter set NL3* is presented for different cases. Lines labelled as “i-conf.,” “g-conf.,” “g*-conf.” or experimental points correspond to the same data as in Fig. 2. Lines including “ $F_{1ij} = 0$ ” or “ $F_{2gj} = 0$ ” show the results neglecting the corresponding F component, as explained in the body text

showing that the difference in magnitude of the kinks for the g-conf and g*-conf is larger when $V_{\text{SO},2g} \neq 0$ than when $V_{\text{SO},2g} = 0$.

We have stated in the previous paragraph that for the three configurations considered, the magnitude of the kink decreases by a similar amount when the small component of the neutron orbital characterising the configuration is neglected. This result indicates that the small component of the valence neutrons will remain essential in the kink formation when considering pairing correlations. This is ensured by the fact that, between the neutron valence orbitals, the $1i_{11/1}$ and $2g_{9/2}$ orbitals have, by far, the highest occupancy probabilities and their small components contribute to the magnitude of the kink by a similar amount.

In the rest of this Subsection, we will attempt to explain why the small component of the Dirac spinors plays such an important role in the kink formation. It will be helpful to consider the contribution of valence neutrons to the central potential $V_{\text{cent}}(r, \epsilon)$ for protons in the Schrödinger-like Eq. (15). (We will assume that, regarding the kink, the impact on the proton SO potential is less relevant). Neutrons do not contribute to the Coulomb potential. Then, assuming that the

meson mass terms in Eqs. (4, 5, 6) are significantly greater than the corresponding Laplacian terms, allowing for an iterative solution, we can write the scalar and vector potentials for protons in a spherical nucleus as

$$S(r) \simeq -\frac{g_\sigma^2}{m_\sigma^{*2}} \left(1 + \frac{1}{m_\sigma^{*2}} \nabla^2 + \dots \right) \rho_S(r), \tag{24}$$

$$V(r) \simeq \frac{g_\omega^2}{m_\omega^2} \left(1 + \frac{1}{m_\omega^2} \nabla^2 + \dots \right) \rho_B(r) + \frac{g_\rho^2}{m_\rho^2} \left(1 + \frac{1}{m_\rho^2} \nabla^2 + \dots \right) \rho_3(r). \tag{25}$$

To clarify the role of the small component of the sp Dirac spinors in the formation of the kink, we first consider the contribution of a single-neutron in the orbital a (with the same occupancy probability for the $2j_a + 1$ states of this orbital) to the proton central potential $V_{\text{cent}}(r, \epsilon)$ in Eqs. (15, 16). We denote this contribution as $V_{\text{cent}}^{n,a}(r, \epsilon)$, and this meaning will remain unchanged in the rest of the work. Let us suppose $\rho_{S,a}(r)$, $\rho_{n,a}(r)$, $\sigma^a(r)$, $\omega_0^a(r)$, $\rho_{0,3}^{n,a}(r)$, $S_a(r)$ and $V_a(r)$ are the contributions of this neutron to the scalar $\rho_S(r)$ and neutron $\rho_n(r)$ densities, the $\sigma(r)$, $\omega_0(r)$, $\rho_{0,3}(r)$ fields, and the scalar $S(r)$ and vector $V(r)$ potentials, respectively. If in Eq. (16) we neglect the relatively small terms including the factor M^{-1} , which are small relativistic contributions, taking into account Eqs. (2) and (3), we can write:

$$V_{\text{cent}}(r, \epsilon) \simeq V_{\text{cent}^*}(r) \equiv S(r) + V(r) \tag{26}$$

and

$$V_{\text{cent}}^{n,a}(r, \epsilon) \simeq V_{\text{cent}^*}^{n,a}(r) \equiv S_a(r) + V_a(r) = g_\sigma \sigma^a(r) + g_\omega \omega_0^a(r) + g_\rho \rho_{0,3}^{n,a}(r). \tag{27}$$

We notice that the potentials $g_\sigma \sigma(\vec{r})$ and $g_\omega \omega_0(\vec{r})$ in Eqs. (2, 3) for protons and neutrons are identical but the potential $\tau_3 g_\rho \rho_{0,3}(\vec{r})$ in (3) is different. To facilitate discussion only, we assume that the meson masses are large enough to allow us to neglect the Laplacian terms in Eqs. (24) and (25). In other words, we consider $S(r)$ and $V(r)$ in the simplest local density approximation (LDA). Then, we can write $V_{\text{cent}^*}^{n,a}(r)$ for protons arising from one neutron in the a orbital as

$$V_{\text{cent}^*}^{n,a}(r) \simeq -\frac{g_\sigma^2}{m_\sigma^{*2}} \rho_{S,a}(r) + \left[\frac{g_\omega^2}{m_\omega^2} - \frac{g_\rho^2}{m_\rho^2} \right] \rho_{n,a}(r). \tag{28}$$

Considering Eqs. (10–12) (and often omitting, for simplicity, the dependence on r in the functions $G_a(r)$ and $F_a(r)$ from

this point onward), we have

$$\begin{aligned}
 V_{\text{cent}^*}^{n,a}(r) &\simeq \left[\frac{g_\omega^2}{m_\omega^2} - \frac{g_\rho^2}{m_\rho^2} \right] \frac{G_a^2 + F_a^2}{4\pi r^2} - \frac{g_\sigma^2}{m_\sigma^{*2}} \frac{G_a^2 - F_a^2}{4\pi r^2} \\
 &= \left[\frac{g_\omega^2}{m_\omega^2} - \frac{g_\rho^2}{m_\rho^2} - \frac{g_\sigma^2}{m_\sigma^{*2}} \right] \frac{G_a^2}{4\pi r^2} \\
 &\quad + \left[\frac{g_\omega^2}{m_\omega^2} - \frac{g_\rho^2}{m_\rho^2} + \frac{g_\sigma^2}{m_\sigma^{*2}} \right] \frac{F_a^2}{4\pi r^2}.
 \end{aligned} \tag{29}$$

It is important to note that adding one neutron to the nucleus in a specific orbital triggers modifications in all orbitals due to the self-consistency or rearrangement effects. These modifications, however, are not considered in Eq. (29). The expression of $V_{\text{cent}^*}^{n,a}(r)$ in this equation represents the modification of $V_{\text{cent}^*}(r)$ in the zeroth order of perturbation theory.

For appropriate functionals used in the RMFA, $\frac{g_\omega^2}{m_\omega^2} - \frac{g_\rho^2}{m_\rho^2} \lesssim \frac{g_\sigma^2}{m_\sigma^{*2}}$ (for example, for the NL3* set $\frac{g_\rho^2/m_\rho^2}{g_\omega^2/m_\omega^2} \simeq 0.134$; i.e., $\frac{g_\rho^2}{m_\rho^2} \ll \frac{g_\omega^2}{m_\omega^2}$). This implies, on the one hand, that the overall contribution of the large component G_a to $V_{\text{cent}^*}^{n,a}(r)$ in Eq. (29) is negative and, on the other hand, that the contributions of G_a to the σ -scalar and ω -vector potentials exhibit opposite signs, resulting in a substantial offset between them. Conversely, contributions of the small component F_a to the σ -scalar and ω -vector potentials in $V_{\text{cent}^*}^{n,a}(r)$ are positive and add constructively to each other.

To compare the magnitudes of the $G_a^2/4\pi r^2$ and $F_a^2/4\pi r^2$ factors in Eq. (29), we have depicted them in Fig. 4 for the NL3* set. It can be seen that inside the nucleus, the factor of $F_a^2/4\pi r^2$ outweighs that of $G_a^2/4\pi r^2$ by roughly five times. This fact strongly enhances the role of the small component of the valence neutron orbitals in lead isotopes in the central potential $V_{\text{cent}}(r, \epsilon)$ in the Schrödinger-like equation (15). Given that $\left| \frac{g_\omega^2}{m_\omega^2} - \frac{g_\rho^2}{m_\rho^2} - \frac{g_\sigma^2}{m_\sigma^{*2}} \right| < \frac{g_\omega^2}{m_\omega^2} - \frac{g_\rho^2}{m_\rho^2} + \frac{g_\sigma^2}{m_\sigma^{*2}}$, in the non-relativistic limit, the absence of the contribution of the small component $F_a(r)$ ($= 0$) to $V_{\text{cent}}(r, \epsilon)$ cannot be compensated with the small contribution due to the renormalisation of the norm of the large component $G_a(r)$ to the unity. Actually, as $\frac{g_\omega^2}{m_\omega^2} - \frac{g_\rho^2}{m_\rho^2} - \frac{g_\sigma^2}{m_\sigma^{*2}} < 0$, the contribution due to this renormalisation will have a sign opposite to that of the term $[...]F_a^2/4\pi r^2$ in Eq. (29). Note that the contribution of the vector ρ -meson to $V_{\text{cent}^*}(r)$ or $V_{\text{cent}^*}^{n,a}(r)$ is quite small compared to that of the vector ω -meson but becomes significant in the factor $\left[\frac{g_\omega^2}{m_\omega^2} - \frac{g_\rho^2}{m_\rho^2} - \frac{g_\sigma^2}{m_\sigma^{*2}} \right]$ of Eq. (29). Consequently, globally, this contribution should not be neglected.

The discussion in the preceding paragraph indicates that, for a given orbital, the contribution of its small component with respect to that of its large component is approximately

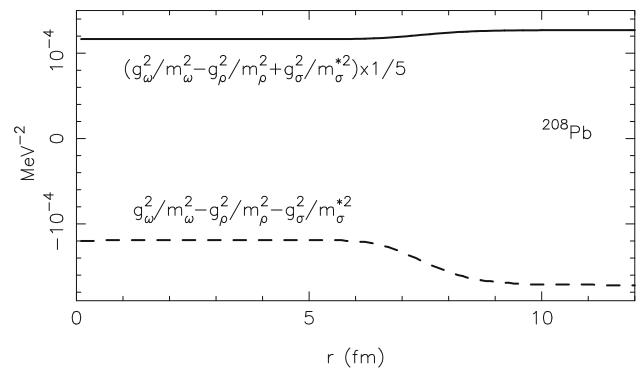


Fig. 4 Factors [...] of $G_a^2/4\pi r^2$ (dashed line) and $F_a^2/4\pi r^2$ (solid line) in Eq. (29), as indicated in the figure, for the ^{208}Pb nucleus with the NL3* parameter set

five times greater for the central potential in the Schrödinger-like equation (15) than for the nucleon density in Eq. (11). This highlights the significant role of the small component of the valence neutron orbitals in the three configurations of lead considered in Fig. 3. It is worth realising that the relevance of the small component $F_a(r)$ on $V_{\text{cent}^*}(r)$ is due, on the one hand, to the different signs of the source terms in the scalar and vector field Eqs. (24, 25) and, on the other hand, to the different signs in front of $F_a^2(r)$ on the relativistic scalar and nucleon densities (see Eqs. (10, 9)).

Concerning the discussion in the two previous paragraphs about the role of the small component $F_a(r)$ of the Dirac spinors on the central potential $V_{\text{cent}}(r, \epsilon)$, it is worth noting that a similar mechanism to the one discussed there is responsible for the saturation of nuclear matter in conventional nuclear relativistic models. We briefly recapitulate this mechanism for symmetric nuclear matter. As the nuclear density increases, $S(r) - V(r)$ and, consequently, $B(r)$ decreases (see Eq. (14)). Then, the absolute value of the small component of the Dirac spinors grows with increasing density (see Eq. (21)). This leads to the scalar density growing more slowly with the nucleon density than this density itself. Consequently, the attractive scalar potential in Eq. (24) exhibits slower growth with nucleon density than the repulsive vector potential in Eq. (25). This difference in growth rates determines the saturation of nuclear matter. Thus, although the magnitude of the small component of the sp Dirac spinors is much smaller than that of the large one (except near the nodes of the latter in finite nuclei), and the small component hardly contributes to the nuclear density, its role in the nuclear saturation mechanism is essential for achieving the saturation of nuclear matter.

The contribution of the term proportional to $F_a^2/4\pi r^2$ in $V_{\text{cent}^*}^{n,a}(r)$ influences the characteristics of the kink for two reasons. Firstly, it affects the r dependence of $V_{\text{cent}^*}^{n,a}(r)$ and, secondly, it reduces the depth of this potential.

It is worth noting that $V_{SO}(r, \epsilon)$ depends, essentially, on the magnitude of $S(r) - V(r)$ (see Eq. (17)). Studying the impact of the small component of the valence neutron orbitals on $S(r) - V(r)$, as we did previously for $S(r) + V(r)$, it is easy to verify that this impact is irrelevant. This implies that $V_{SO}(r, \epsilon)$ hardly depends on the small component of those orbitals.

3.2.1 Comparison between the kinks of two configurations

According to the previous paragraph, the small components of the valence neutrons orbitals $1i$ and $2g$ affect, essentially, the central potential $V_{cent}(r, \epsilon)$. Then, to understand the different magnitudes of the kink in lead isotopes for two configurations considered previously, we can compare the contribution to the central potential $V_{cent^*}(r)$ of one neutron in each of the two orbitals (a and b) that distinguish the configurations. The difference between these two contributions, $\delta V_{cent^*}^{n,a-b}(r)$, will be mainly responsible for the different kinks in the two cases considered. We can write

$$\delta V_{cent^*}^{n,a-b}(r) \simeq \left[\frac{g_\omega^2}{m_\omega^2} - \frac{g_\rho^2}{m_\rho^2} - \frac{g_\sigma^2}{m_\sigma^{*2}} \right] \left[\frac{G_a^2}{4\pi r^2} - \frac{G_b^2}{4\pi r^2} \right] + \left[\frac{g_\omega^2}{m_\omega^2} - \frac{g_\rho^2}{m_\rho^2} + \frac{g_\sigma^2}{m_\sigma^{*2}} \right] \left[\frac{F_a^2}{4\pi r^2} - \frac{F_b^2}{4\pi r^2} \right]. \tag{30}$$

To compare the magnitude of the small and large components of the valence neutron orbitals $1i$ and $2g$, we have depicted in Fig. 5 the quantities F_a^2/r^2 and $-G_a^2/r^2$ as functions of r for these orbitals. (The negative sign in $-G_a^2/r^2$ is used for clarity in the figure, and it will also prove beneficial for subsequent analysis). It is seen that the magnitude of $G_a^2(r)$ can exceed that of $F_a^2(r)$ by a factor greater than fifteen. The substantial disparities between the large components of the two orbitals of an SO doublet are essentially due to the SO interaction.

Next, we analyse the impact of adding one neutron to the valence orbitals $1i$ or $2g$ of the ^{208}Pb nucleus on the nuclear charge radius. To accomplish this, we evaluate the contribution of this neutron to the proton central potential $V_{cent}(r, \epsilon)$. This contribution is approximated, first, by $V_{cent^*}^{n,a}(r)$ from Eq. (27). We consider the i -conf, g -conf and g^* -conf. The mean fields in Eq. (27) are obtained by solving numerically the corresponding field Eqs. (4–6). The source terms in these equations are given by Eqs. (10–12), considering only the contribution of the valence neutron in the orbitals $1i_{11/2}$, $2g_{9/2}$ or $2g_{7/2}$, depending on the configuration under consideration. These orbitals are assumed to be identical to those of ^{208}Pb . (Quantitatively, it would not be significant difference if we choose those orbitals from the ^{209}Pb nucleus).

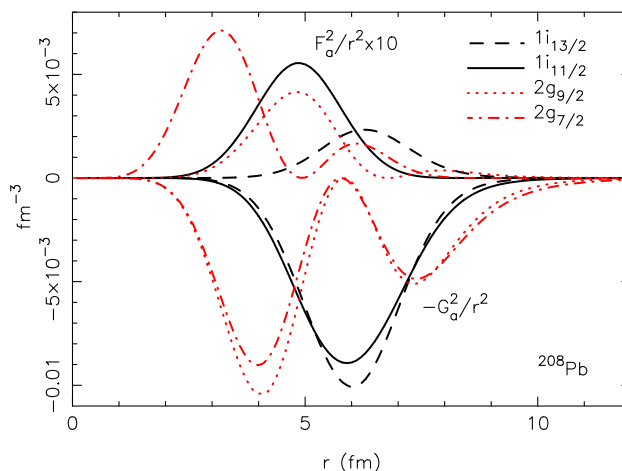


Fig. 5 The quantities $-G_a^2/r^2$ (negative) and F_a^2/r^2 (positive) corresponding to the orbitals $1i_{13/2}$ (full), $1i_{11/2}$ (empty) and $2g$ (empty) in the ^{208}Pb nucleus, as indicated in the figure, for the NL3* parameter set

Before analysing the cases studied in this work with the complete model, which includes the SO interaction for all orbitals, we first discuss the simplest cases where the SO interaction is neglected for the $1i$ orbitals and later for the $2g$ orbitals.

If we consider the SO partner orbitals $1i_{13/2}$ (full) and $1i_{11/2}$ (empty), and neglect their SO interaction ($\epsilon_{1i_{13/2}} = \epsilon_{1i_{11/2}}$), the results for the contributions of the large G_a and small F_a components of these orbitals to $V_{cent^*}^{n,a}(r)$ shown in Fig 6 are easy to interpret. We observe that the contributions of $G_{1i_{13/2}}$ and $G_{1i_{11/2}}$ are practically identical to each other, as expected for these SO partners, and the first addend in Eq. (30) is negligible. The contribution of the small component $F_{1i_{13/2}}$ is notably less relevant than the contribution of $F_{1i_{11/2}}$. Therefore, there is a significant difference between the complete contribution of the orbital $1i_{13/2}$, $V_{cent^*}^{n,1i_{13/2}}(r)$, and that of the orbital $1i_{11/2}$, $V_{cent^*}^{n,1i_{11/2}}(r)$. This difference is essentially due to the second addend in Eq. (30), which depends on the small components $F_{1i_{13/2}}$ and $F_{1i_{11/2}}$.

In Fig. 6, the minimum of $V_{cent^*}^{n,1i_{11/2}}(r)$ is shallower than that of $V_{cent^*}^{n,1i_{13/2}}(r)$ and is placed to its right. This indicates that neutrons in the $1i_{11/2}$ orbital will lead to a larger nuclear charge radius than those in the $1i_{13/2}$ orbital (as shown in Fig. 2). Indeed, Fig. 6 suggests that the impact of neutrons in the $1i_{13/2}$ orbital, through its $F_{1i_{13/2}}$ component, on the nuclear charge radius will be quite limited (as confirmed numerically), since the contribution of this component to $V_{cent^*}^{n,1i_{13/2}}(r)$ is relatively small. Essentially, this contribution slightly reduces the depth of its minimum.

Figure 7 shows the contributions of a single-neutron to $V_{cent^*}^{n,a}(r)$ from the large G_a and small F_a components of the orbitals $1i_{13/2}$ (full) and $1i_{11/2}$ (empty) when considering the

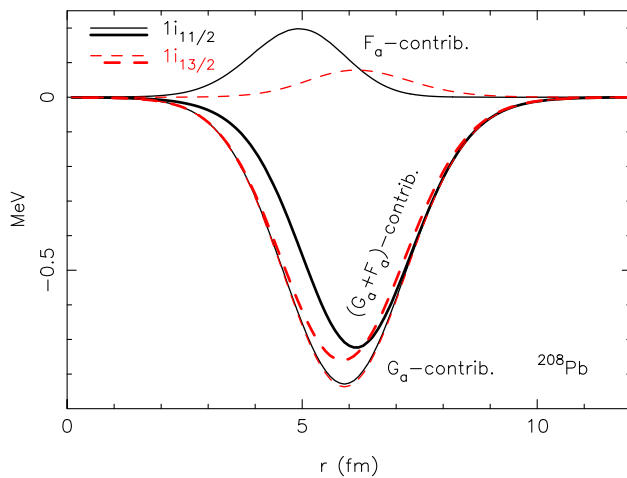


Fig. 6 Contributions of a single-neutron in the a orbital to $V_{\text{cent}}^{n,a}(r)$ from the large (G_a), small (F_a) and both ($G_a + F_a$) components with the NL3* parameter set, assuming $V_{\text{SO},li}(r, \epsilon) = 0$. The a orbital can either represent the (full) orbital $1i_{13/2}$ or the (empty) orbital $1i_{11/2}$ of the ^{208}Pb nucleus. The thinner lines with negative values represent the contributions of the G_a components, and the thinner lines with positive values represent those of the F_a components. The thicker lines represent the total contributions from the a orbitals. All contributions were obtained numerically from Eq. (27). The contributions of the mean fields in this equation were determined by solving the field Eqs. (4–6) with the appropriate source terms. In the LDA, the contributions of a single-neutron to $V_{\text{cent}}^{n,a}(r)$ from G_a and F_a reduce to [...] G_a^2/r^2 and [...] F_a^2/r^2 in Eq. (29), respectively

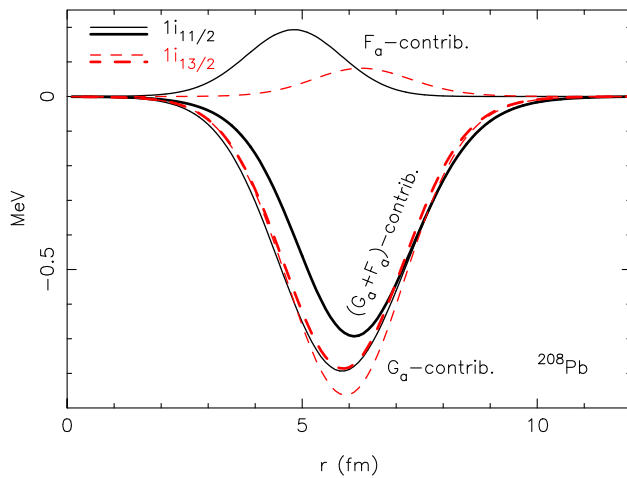


Fig. 7 The same as Fig. 6, but considering $V_{\text{SO},li}(r, \epsilon) \neq 0$

SO interaction for these states. We have contributions qualitatively similar to those obtained when $V_{\text{SO},li} = 0$. However, the contributions of the large components of these orbitals exhibit slight disparities from each other. For the valence neutrons in the $1i_{11/2}$ orbital, i -conf, it can be seen in Fig. 2 that the magnitude of the kink for $V_{\text{SO},li} \neq 0$ is almost identical to that for $V_{\text{SO},li} = 0$. Regarding the kink, the subtle differences between the contributions of this orbital to $V_{\text{cent}}^{n,a}(r)$ in these two cases appear to offset each other.

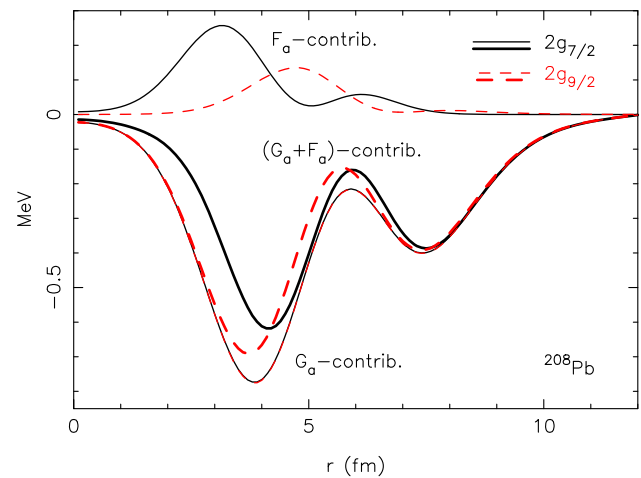


Fig. 8 The same as Fig. 6, but for the $2g_{9/2}$ and $2g_{7/2}$ (empty) orbitals of the ^{208}Pb nucleus, taking $V_{\text{SO},2g}(r, \epsilon) = 0$: Contributions of one neutron in the a orbital to $V_{\text{cent}}^{n,a}(r)$ from the large G_a (thinner lines with negative values), small F_a (thinner lines with positive values) and both ($G_a + F_a$) (thicker lines) components

The contributions from a single valence neutron in the $1i$ orbitals of the ^{208}Pb nucleus to $V_{\text{cent}}^{n,1i_j}(r)$ discussed above do not account for self-consistent or rearrangement effects due to the perturbation of the valence neutron on other occupied orbitals. However, we will see that this perturbation is important and will contribute significantly to $V_{\text{cent}}^{n,a}(r)$. Therefore, conclusions about the contribution of valence neutrons to $V_{\text{cent}}^{n,a}(r)$, reached under the assumption of ignoring self-consistent effects, must be reconsidered when these effects are taken into account.

Now, we consider the $2g$ states and neglect their SO interactions as we did previously for the $2i$ states. In this case, the $G_{2g_{9/2}}$ and $G_{2g_{7/2}}$ functions are also practically identical to each other. Consequently, similarly to what happened previously for the $1i$ states, the different magnitude of the kink for the cases “ g -conf, $V_{\text{SO},2g} = 0$ ” and “ g^* -conf, $V_{\text{SO},2g} = 0$ ” in Fig. 2 is almost entirely due to the difference between the $F_{2g_{9/2}}$ and $F_{2g_{7/2}}$ functions. The contributions to $V_{\text{cent}}^{n,2g_j}(r)$ of these two components can be appreciated in Fig. 8. The contribution of $F_{2g_{7/2}}$ (with $j = j_-$) is quite significant and larger than that of $F_{2g_{9/2}}$ (with $j = j_+$) for small values of r . Due to the contribution of $F_{2g_{7/2}}$, the minimum of $V_{\text{cent}}^{n,2g_{7/2}}(r)$ becomes shallower than that of the $V_{\text{cent}}^{n,2g_{9/2}}(r)$ and shifts to its right. Thus, it is evident that in the case $V_{\text{SO},2g} = 0$, due to the effect of the small components, the orbital $2g_{7/2}$ is more kinky than the orbital $2g_{9/2}$, as observed in Fig. 2.

To understand the different magnitudes of the kinks shown in Fig. 2 for the g -conf and g^* -conf when $V_{\text{SO},2g} \neq 0$, we have computed $V_{\text{cent}}^{n,2g_{9/2}}(r)$ and $V_{\text{cent}}^{n,2g_{7/2}}(r)$ in this scenario. The results are presented in Fig. 9. It can be seen that the contributions of the small components $F_{2g_{9/2}}$ and $F_{2g_{7/2}}$

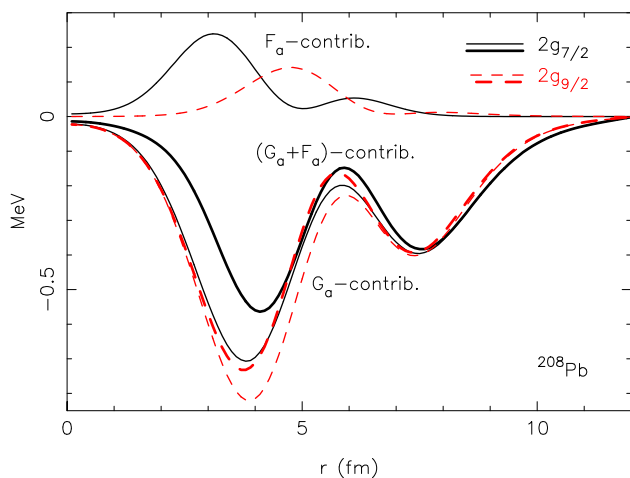


Fig. 9 The same as Fig. 8, but considering $V_{SO,2g}(r, \epsilon) \neq 0$

closely resemble those observed when $V_{SO,2g} = 0$ in Fig. 8. Now, for $V_{SO,2g} \neq 0$, the components $G_{2g_{9/2}}$ and $G_{2g_{7/2}}$ exhibit significant differences between them (refer to Fig. 5). Consequently, their respective contributions to $V_{cent}^{n,2g_{9/2}}(r)$ and $V_{cent}^{n,2g_{7/2}}(r)$ also differ from each other, as illustrated in Fig. 9. Comparison of these results with the corresponding ones in Fig. 8 reveals that the contribution of $G_{2g_{7/2}}$ is more favourable to the kink when $V_{SO,2g} \neq 0$ than when $V_{SO,2g} = 0$, while that of $G_{2g_{9/2}}$ is less favourable to the kink when $V_{SO,2g} \neq 0$ than when $V_{SO,2g} = 0$. This observation explains why the kink magnitudes for the g -conf and g^* -conf differ more from each other when $V_{SO,2g} \neq 0$ than when $V_{SO,2g} = 0$ (see Fig. 2).

Now, we discuss the more intricate cases of the i -conf and g -conf. In Fig. 10, we depict the contributions to $V_{cent}^{n,a}(r)$ of one neutron in the orbitals $1i_{11/2}$ (i -conf) and $2g_{9/2}$ (g -conf). It can be seen that the contributions of the large components are quite different from each other. In contrast, those of the small components are rather similar (as expected for two members of a pseudospin doublet [37–39]). Consequently, the significant difference in the magnitude of the kink for the i -conf and g -conf should be primarily attributed to the substantial disparity between the functions $G_{1i_{11/2}}$ and $G_{2g_{9/2}}$ in Eq. (30).

For the two orbitals considered, *the contributions of the small components are not negligible in comparison to those of the large components* and significantly reduce the depth of $V_{cent}^{n,a}(r)$. This effect will contribute to an increase in the nuclear charge radius for both configurations. The shift of the minimum of $V_{cent}^{n,1i_{11/2}}(r)$ due to the contribution of the small component $F_{1i_{11/2}}$ is notable and also favours the increase of the nuclear charge radius. The displacement of the first minimum of $V_{cent}^{n,2g_{9/2}}(r)$ due to the contribution of $F_{2g_{9/2}}$ is smaller and occurs in the opposite direction compared to that of $V_{cent}^{n,1i_{11/2}}(r)$. While this displacement will have a slight

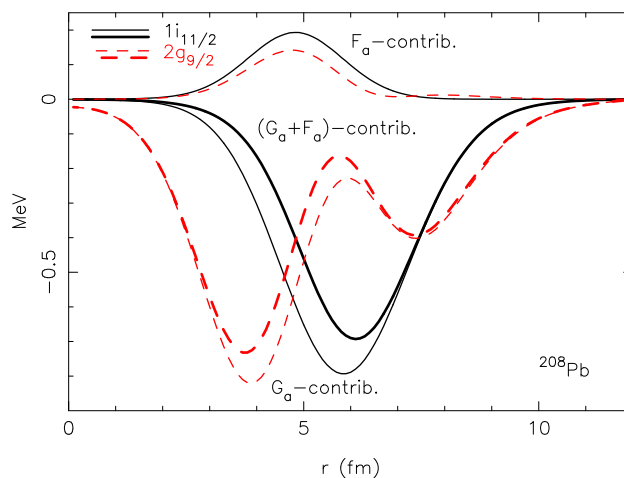


Fig. 10 The same as Figs. 6, 7, 8 and 9, but for the $1i_{11/2}$ and $2g_{9/2}$ orbitals, taking $V_{SO,1i,2g}(r, \epsilon) \neq 0$

decreasing effect on the charge radius, its impact should be smaller than the opposing effect resulting from the reduction of the depth of $V_{cent}^{n,2g_{9/2}}(r)$. The net effect of the $F_{2g_{9/2}}$ contribution on the charge radius, including self-consistent effects, is a noticeable increase in magnitude, as illustrated in Fig. 3. Accurate numerical calculations indicate that neutrons in the $F_{1i_{11/2}}$ orbital are approximately one-third more efficient in increasing the nuclear charge radius than those in the $F_{2g_{9/2}}$ orbital (see Fig. 3).

Upon comparing the overall potentials $V_{cent}^{n,1i_{11/2}}(r)$ and $V_{cent}^{n,2g_{9/2}}(r)$ in Fig. 10, it appears that the first potential is more likely to favour an increase in the nuclear charge radius than the second potential. This intuition is further supported by the results depicted in Fig. 2. The two wells of the second potential will attract protons towards them. The first well is deeper than the second. So, at first glance, it seems this feature will be important for the dominance of the former over the latter. However, as we will see below, self-consistent effects increase the relative relevance of the second well compared to the first one and must be considered. These self-consistent effects are practically independent of the SO interaction of the valence neutrons.

Comparing the results of Figs. 7 and 9 for the contributions to $V_{cent}^{n,a}(r)$ from the large and small components of the neutron orbitals $1i$ and $2g$ with the corresponding quantities $-G_a^2/r^2$ and F_a^2/r^2 in Fig. 5 can provide valuable insights. It is clear that the (negative) contribution of the large component to $V_{cent}^{n,a}(r)$ is roughly proportional to $-G_a^2/r^2$, and the (positive) contribution of the small component is roughly proportional to F_a^2/r^2 , as indicated by Eq. (29). That is, for determining the contributions of G_a and F_a to the potential $V_{cent}^{n,a}(r)$, separately, the LDA works quite well. However, the probability density corresponding to one neutron in the orbital a , $\rho_{n,a}(r)$, is proportional to

$(G_a^2 + F_a^2)/r^2$, while we have seen that for the NL3* set, in the inner part of the nucleus, $V_{\text{cent}^*}^{n,a}(r)$ is, roughly, proportional to $(-G_a^2 + 5 \times F_a^2)/r^2$ (see Eq. (29) and Fig. 4, and note the different relative signs of the contributions of G_a and F_a to $\rho_{n,a}(r)$ and $V_{\text{cent}^*}^{n,a}(r)$). Therefore, as $5 \times F_a^2$ cannot be considered negligible, in general, compared to G_a^2 , $V_{\text{cent}^*}^{n,a}(r)$ cannot be assumed to be proportional to $\rho_{n,a}(r) \propto (G_a^2 + F_a^2)/r^2$. Consequently, in general, the LDA will not be adequately satisfied when considering the contribution of the entire a orbital to $V_{\text{cent}^*}^{n,a}(r)$ (we will see below that self-consistent effects aggravate this failure of LDA). This result highlights the impossibility of accurately determining the contribution of neutrons in a given orbital a to $V_{\text{cent}^*}(r)$ as a magnitude proportional to $\rho_{n,a}(r)$. Such a limitation in RMFA hampers the ability to predict the behaviour of the nuclear charge rms radius for the i -conf, g -conf, or g^* -conf by directly analysing the valence neutron densities in the orbitals $1i_{11/2}$, $2g_{9/2}$, or $2g_{7/2}$, respectively.

3.2.2 Self-consistency effects of the valence neutrons in lead isotopes with $N > 126$ on the proton central potential in the Schrödinger-like equation

Above, we examined the direct effects of the valence neutrons in lead isotopes on the proton central potential $V_{\text{cent}}(r, \epsilon)$, approximated by $V_{\text{cent}^*}(r)$. Next, we will study the secondary self-consistent effects of these neutrons on this potential, which arise from their perturbation on other occupied orbitals. We also begin by considering the approximation $V_{\text{cent}}(r, \epsilon) \simeq V_{\text{cent}^*}(r)$. The changes in $V_{\text{cent}^*}(r)$ produced by the $N - 126$ ($N > 126$) valence neutrons in the ${}^A\text{Pb}$ nucleus, including both direct and secondary effects, denoted as $\delta V_{\text{cent}^*}(r)$, can be assessed by comparing the potential $V_{\text{cent}^*}(r)$ in ${}^A\text{Pb}$ ($A > 208$) and ${}^{208}\text{Pb}$ after convergence. For ${}^{214}\text{Pb}$ (the largest lead isotope we consider), we have

$$\delta V_{\text{cent}^*}(r) = [V_{\text{cent}^*}(r)]_{214\text{Pb}} - [V_{\text{cent}^*}(r)]_{208\text{Pb}}. \quad (31)$$

In Fig. 11, we plot $\delta V_{\text{cent}^*}(r)$ for the i -conf, g -conf and g^* -conf. In the absence of self-consistent effects, $\delta V_{\text{cent}^*}(r)$ would be identical to six times (once per neutron exceeding $N = 208$ until $N = 214$) the potential $V_{\text{cent}^*}^{n,a}(r)$ corresponding to the configuration considered, as shown in Fig. 9 for the g -conf and g^* -conf and in Fig. 10 for the g -conf and i -conf.

The self-consistent effects in $\delta V_{\text{cent}^*}(r)$ for the ${}^{214}\text{Pb}$ nucleus can be measured as the difference $\delta V_{\text{cent}^*}(r) - 6 \times V_{\text{cent}^*}^{n,a}(r)$. In Fig. 12, we depict this difference for the three configurations considered in this work, revealing that self-consistency effects are very significant in all three cases. It can be seen that self-consistency effects increase the potential $\delta V_{\text{cent}^*}(r)$ between the centre and surface of the nucleus, roughly coinciding the peak with the maximum of the small component contribution corresponding to the considered configuration (see Figs. 9 and 10). However, self-consistency

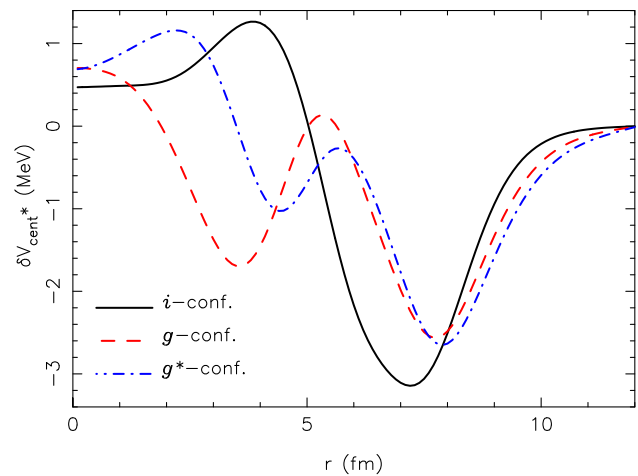


Fig. 11 The quantity $\delta V_{\text{cent}^*}(r)$ for protons when six neutrons are added to the ${}^{208}\text{Pb}$ nucleus to get ${}^{214}\text{Pb}$ in the indicated configurations. We have used the NL3* parameter set. Note that $\delta V_{\text{cent}^*}(r)$ is independent from the proton orbital

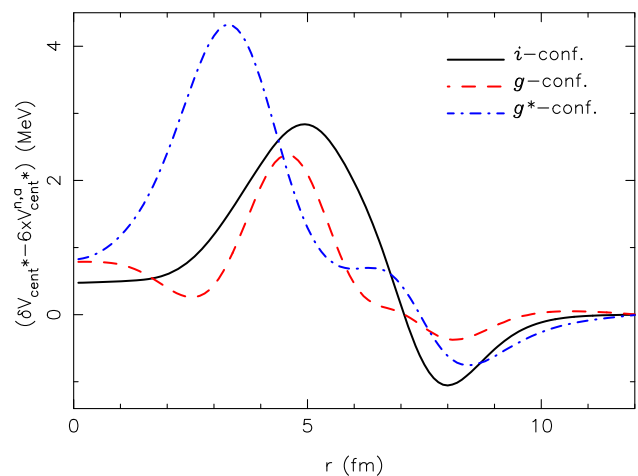


Fig. 12 Variation of $\delta V_{\text{cent}^*}(r)$ due to the secondary self-consistent effects for protons when six neutrons are added to the ${}^{208}\text{Pb}$ nucleus to get ${}^{214}\text{Pb}$ in the indicated configurations. We have used the NL3* set

effects decrease $\delta V_{\text{cent}^*}(r)$ in the surface region, around 7–8 fm, approaching the more significant variation towards the outermost minimum of the large component or total orbital contribution for the considered configuration.

These results indicate that the contribution of self-consistency effects to $\delta V_{\text{cent}^*}(r)$ amplifies the direct contribution (given by $6 \times V_{\text{cent}^*}^{n,a}(r)$) of the small components and that of the big components for large values of r . Consequently, self-consistency strongly favours the emergence of the kink in all three configurations of lead ($A > 208$) considered, enhancing the direct effects of the valence neutrons on the proton core that favour the kink formation. Hence, an accurate determination of the impact of valence neutrons on the charge radius of lead for $N > 126$ requires the inclusion of self-consistency. As mentioned above, self-consistent

effects are practically independent of the SO interaction of the valence neutrons.

To understand the modifications in the potential $V_{\text{cent}^*}(r)$ due to the self-consistency effects, it is worth keeping in mind that the volume element in spherical coordinates corresponding to dr is proportional to $r^2 dr$. This behaviour enhances the relative relevance of $V_{\text{cent}^*}(r)$ in the outer part of the nucleus compared to the inner part because nucleons beneficial for a given dr of a larger volume ($\propto r^2 dr$) as r increases.

If, hypothetically, neutrons were added to the ^{208}Pb nucleus in the $1i_{11/2}$ orbital (in the i -conf), a (direct) potential almost identical to $V_{\text{cent}^*}^{n,1i_{11/2}}(r)$ would be generated initially for protons with each neutron added (see Fig. 10). This potential would show a minimum (well) around $r \simeq 6$ fm, attracting protons from the nucleus's inner part. The movement of these protons towards the well would increase the nuclear potential in the inner part of the nucleus (making it less negative) and would decrease it on the right of the well, shifting the minimum of the well to larger values of r . In turn, this well shift would promote greater proton movement at larger values of r , further increasing the displacement of the well. This self-consistent process would continue until equilibrium is reached. The ultimate outcome would be that, if six neutrons were added to the ^{208}Pb nucleus in the $1i_{11/2}$ orbital, the potential $V_{\text{cent}^*}(r)$ would vary as $\delta V_{\text{cent}^*}(r)$ depicted in Fig. 11.

If, hypothetically, neutrons were added to the ^{208}Pb nucleus in the $2g_{9/2}$ orbital (in the g -conf), a potential almost identical to $V_{\text{cent}^*}^{n,2g_{9/2}}(r)$ would be generated for protons with each neutron added (see Fig. 10). This potential would exhibit two minima, two wells, attracting protons from their left sides. However, the internal well would not accumulate protons because it would lose them on its right due to the attraction of the outer well (with a larger volume effect $\propto r^2$). Thus, the proton potential would increase around the internal well and decrease on the right of the external well. This explains how the potential $V_{\text{cent}^*}(r)$ is modified by self-consistent effects when transitioning from ^{208}Pb to ^{214}Pb . This modification is illustrated by $\delta V_{\text{cent}^*}(r)$ in Fig. 11.

The case of adding neutrons to the ^{208}Pb nucleus in the $2g_{7/2}$ orbital (in the g^* -conf), would be very similar to the case of adding neutrons to the $2g_{9/2}$ orbital previously discussed.

The impact of the SO interaction of the valence neutrons in the self-consistent effects is negligible for the three configurations considered. If a figure similar to Fig. 11 were drawn for the cases in which the SO interaction is neglected, alternatively, for the $1i$ and $2g$ orbitals, only the direct effects of the SO interaction would be clearly observable. These effects can be appreciated by comparing Figs. 6 and 7 for the $1i$ states and Figs. 8 and 9 for the $2g$ states. The potential $\delta V_{\text{cent}^*}(r)$ would barely decrease the depth of its mini-

um (around $r \simeq 7.2$ fm) for the i -conf, whereas it would slightly increase (decrease) around its first minimum for the g -conf (g^* -conf). These consequences of the SO interaction of the valence neutrons on $V_{\text{cent}^*}(r)$ allow us to explain its effects on the charge radius isotope shift on the lead family, as depicted in Fig. 2. That is, The SO interaction hardly influences the kink effect for the i -conf, whereas it slightly decreases (increases) its magnitude for the g -conf (g^* -conf).

The impact of the Coulomb potential energy on self-consistent effects in the three configurations discussed above is perceptible but not significant.

3.2.3 Effects of the relativistic terms of the central potential in the Schrödinger-like equation on the kink

The potential $V_{\text{cent}^*}(r)$ considered above comprises only the term $S(r) + V(r)$ from the central potential $V_{\text{cent}}(r, \epsilon)$ in the Schrödinger-like equation Eq. (16). The remaining terms of this potential, which include the small factor $1/M$ and constitute small relativistic contributions, are yet to be considered. To assess their impact on the kink, we now consider the complete potential $V_{\text{cent}}(r, \epsilon)$. The behaviour of the kink essentially depends on how this potential varies when neutrons are added to the lead nucleus for $N > 126$. Therefore, we define $\delta V_{\text{cent}}(r, \epsilon)$ similarly to $\delta V_{\text{cent}^*}(r)$ as

$$\delta V_{\text{cent}}(r, \epsilon) = [V_{\text{cent}}(r, \epsilon)]_{214\text{Pb}} - [V_{\text{cent}}(r, \epsilon)]_{208\text{Pb}}. \quad (32)$$

It is important to emphasise that $\delta V_{\text{cent}}(r, \epsilon)$ depends not only on the nuclear configuration considered, as $\delta V_{\text{cent}^*}(r)$, but also on the energy of the orbital on which it acts. In Fig. 13, we illustrate $\delta V_{\text{cent}}(r, \epsilon)$ corresponding to the proton orbital $1s_{1/2}$ for the three configurations of ^{214}Pb under consideration. Upon comparing this figure with Fig. 11, it becomes evident that the impact of relativistic corrections of order $1/M$ on $\delta V_{\text{cent}}(r, \epsilon)$ is relatively small. As the energy of a state approaches that of the Fermi level, its binding energy decreases and the dependence of $\delta V_{\text{cent}}(r, \epsilon)$ on this energy becomes less relevant. To show the evolution of $\delta V_{\text{cent}}(r, \epsilon)$ from the $1s_{1/2}$ to the $1g_{9/2}$ orbital, we have depicted this potential for several orbitals in Figs. 13, 14 and 15.

From the results of these figures, we can expect that, for the NL3* parameter set, the i -conf will exhibit a more pronounced kink than the g^* -conf, and the g^* -conf will display a more prominent kink than the g -conf for the rms of the all nodeless proton orbitals with the exception, perhaps, of the $1s$ orbital. (We will refer to this statement below). This orbital is special because is highly localised in the internal part of the nucleus, and its behaviour depends mainly on the characteristics of the potential $V_{\text{cent}}(r, \epsilon)$ in this region. Orbitals with nodes exhibit a more intricate behaviour (although understandable) than their nodeless counterparts. However, they barely contribute to the kink [4, 11].

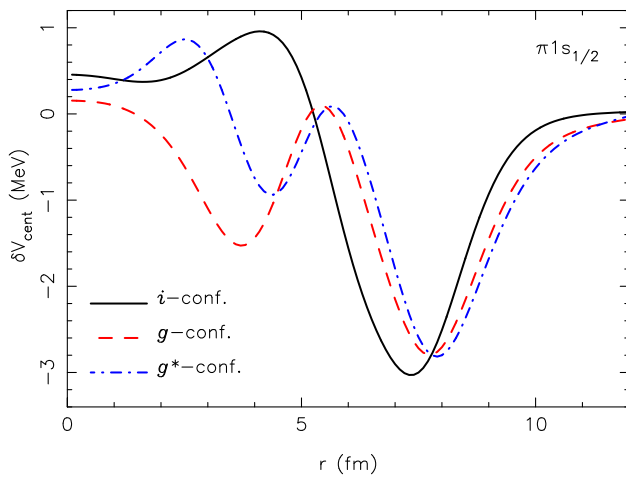


Fig. 13 Variation $\delta V_{\text{cent}}(r, \epsilon)$ for protons in the $1p_{3/2}$ orbital when six neutrons are added to the ^{208}Pb nucleus to get ^{214}Pb in the indicated configurations. It has been used the NL3* parameter set

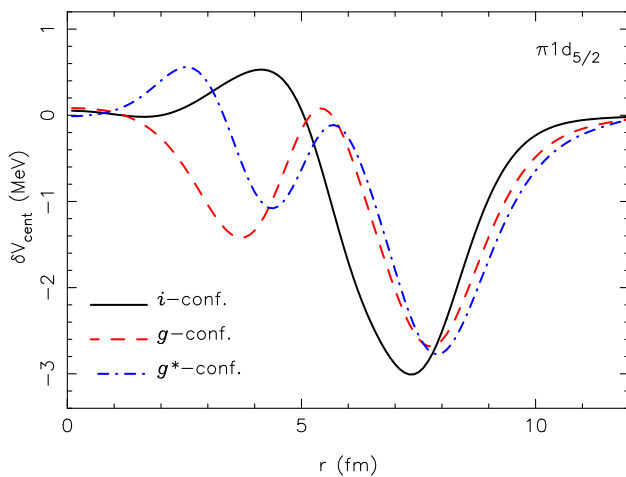


Fig. 14 The same as Fig. 13, but for the proton orbital $1d_{5/2}$

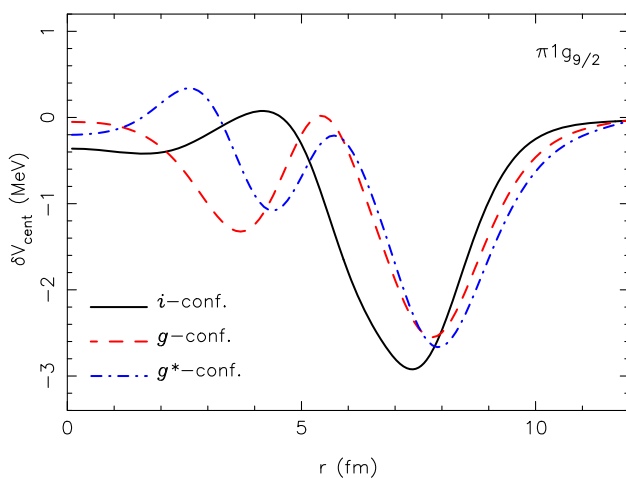


Fig. 15 The same as Fig. 13, but for the proton orbital $1g_{9/2}$

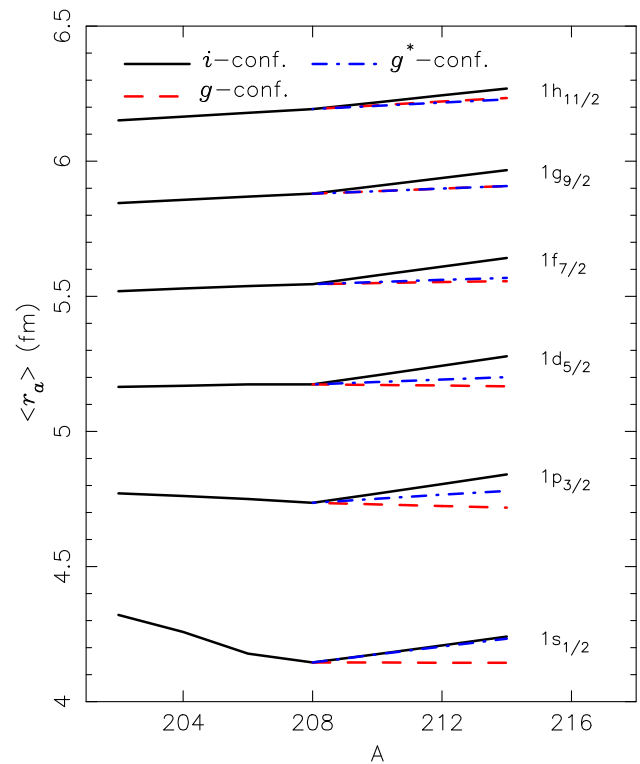


Fig. 16 The rms radii $\langle r_a \rangle$ of the nodeless ($n = 1$) proton orbitals with $j = j_+$ for the lead isotopes are presented as a function of the mass number A . For $N > 126$, the neutrons are assumed to occupy one of the levels $\nu 1i_{11/2}$ (i -conf.), $\nu 2g_{9/2}$ (g -conf.) or $\nu 2g_{7/2}$ (g^* -conf.). The results correspond to the NL3* set. For the states with $j = j_-$, the values of $\langle r_a \rangle$ follow a similar trend to those in the figure but are placed slightly below them, since they are smaller, and are not depicted

To scrutinise the behaviour of the rms radii of nodeless orbitals further, we present in Fig. 16 the rms radii of the nodeless protons orbitals with $j = j_+$ in lead isotopes, plotted against the mass number A for the three configurations considered in this work. It can be observed that the above statement regarding the relative magnitude of the kinks in the i -conf, g -conf and g^* -conf holds for all nodeless orbitals but is more evident for orbitals with $1 \leq l_a \leq 3$. The results for the states with $j = j_-$ are similar to those with $j = j_+$.

To better understand the behaviour of the rms radii $\langle r_a \rangle$ depicted in Fig. 16, we have drawn in Figs. 17, 18 and 19 the probability density variations, $\delta\rho_{p,a}(r)$, corresponding to the proton orbitals considered in Figs. 13, 14 and 15 as the lead isotope changes from ^{208}Pb to ^{214}Pb :

$$\delta\rho_{p,a}(r) = [\rho_{p,a}(r)]_{214\text{Pb}} - [\rho_{p,a}(r)]_{208\text{Pb}}. \quad (33)$$

It is worth noting that the variation of the mean-square radius of the orbital a from ^{208}Pb to ^{214}Pb can be written as

$$\delta\langle r_a^2 \rangle \equiv \delta\langle a | r^2 | a \rangle = 4\pi \int_0^\infty \delta\rho_{p,a}(r) r^4 dr. \quad (34)$$

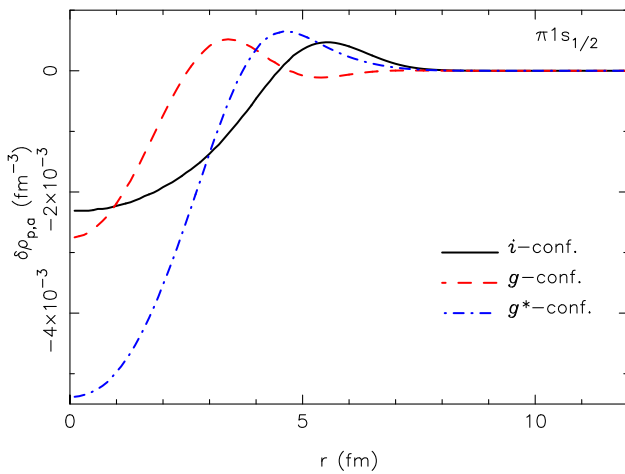


Fig. 17 Variation of the proton probability density distribution $\delta\rho_{1s}(r)$, as defined by Eq. (33), when six neutrons are added to the ^{208}Pb nucleus to get ^{214}Pb in the indicated configuration. The NL3* parameter set was used

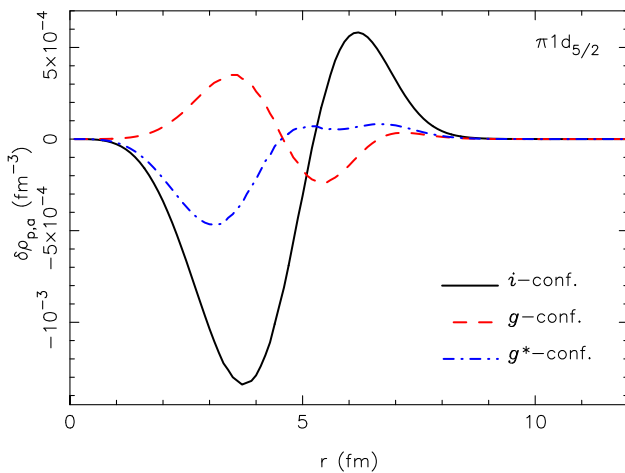


Fig. 18 The same as Fig. 17, but for the proton orbital $1d_{5/2}$

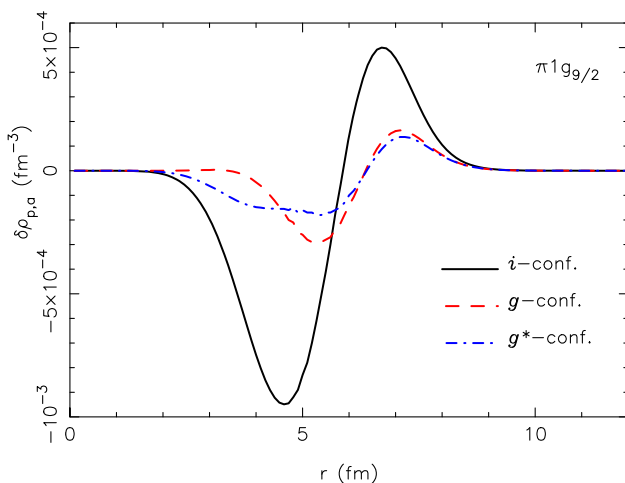


Fig. 19 The same as Fig. 17, but for the proton orbital $1g_{9/2}$

For the *i*-conf, the behaviour of $\delta\rho_{p,a}(r)$ is easy to understand in all cases drawn in Figs. 17, 18 and 19 (similar results are found in Fig. 4 of [23]). To minimise the potential energy, the self-consistency procedure compels $\delta\rho_{p,a}(r)$ to decrease in the inner region of the nucleus, where $\delta V_{\text{cent}}(r, \epsilon)$ attains its largest values, and to increase in the outer region, where it is strongly negative. Consequently, the rms radius of all nodeless proton orbitals increases as neutrons are added to the lead nucleus in the $1i_{11/2}$ orbital for $N > 126$, as shown in Fig. 16. (Note that the spherical element of volume corresponding to dr is $\propto r^2 dr$, and this effect is not considered in Figs. 17, 18 and 19).

It seems clear that for a hypothetical nodeless proton orbital with a density distribution $\rho_{p,a}(r)$ reaching its maximum for $r \gtrsim 8$ fm, the potential $\delta V_{\text{cent}}(r, \epsilon)$ for the *i*-conf would pull protons towards the inner part of the nucleus, leading to $\delta(r_a^2) < 0$. Consequently, for higher values of the orbital angular momentum, l_a , one can expect $\delta(r_a^2)$ to increase with A less rapidly as l_a increases. This trend is subtly noticeable in Fig. 16 for the states with $l_a \geq 1$.

For the *g*-conf and *g**-conf, the presence of the two wells in $\delta V_{\text{cent}}(r, \epsilon)$ adds complexity to the behaviour of $\delta\rho_{p,a}(r)$ compared to the corresponding results for the *i*-conf.

For the *g**-conf, the influence of the external well prevails over that of the internal one for all nodeless orbitals, as shown in Figs. 17, 18 and 19, leading to a slight decrease in $\delta\rho_{p,a}(r)$ in the inner part of the nucleus and a corresponding increase in its outer part. As a result, the rms radius of all nodeless proton orbitals increases slightly when neutrons are added to the lead isotopes in the $2g_{7/2}$ level for $N > 126$, and a tiny kink also appears for the orbitals with $l_a \leq 2$ in the *g**-conf, as shown in Fig. 16.

For the *g*-conf, the influence of the internal well, which is deeper than the corresponding well in the *g**-conf, predominates over that of the external one for the inner nodeless proton orbitals with $l_a \leq 2$. Consequently, $\delta\rho_{p,a}(r)$ increases in the vicinity of the internal well and decreases correspondingly to the left and right of this well for the orbital $1s$, and only on the right for orbitals with $l_a = 1, 2$. Then, as A increases from $A = 208$, $\langle r_{1s} \rangle$ remains practically constant, while $\langle r_{1p_{3/2}} \rangle$ and $\langle r_{1d_{5/2}} \rangle$ slightly decrease, as depicted in Fig. 16. The behaviour of $\delta\rho_{p,1s}(r)$ is special because, due to the absence of the centrifugal barrier for the $1s$ orbital, $\rho_{p,1s}(r)$ attains relatively large values in the centre of nucleus. Thus, the high proton density of this orbital in the inner part of the nucleus enables a greater migration compared to other orbitals, from the inner part of the nucleus towards a more external region where $\delta V_{\text{cent}}(r, \epsilon)$ reaches significant negative values. For orbitals with $l_a \geq 4$, the influence of the external potential well of $\delta V_{\text{cent}}(r, \epsilon)$ predominates over that of the internal one, causing the proton density $\delta\rho_{p,a}(r)$ to rise near the external well at the expense of the more internal

proton density. As a result, $\langle r_a \rangle$ increases as A increases for $A > 208$, although it is insufficient to form a kink.

Considering the preceding discussion relative to the g -conf and g^* -conf, it is clear that for these configurations there is a competition between the two wells of $\delta V_{\text{cent}}(r, \epsilon)$, each vying to attract protons. *This rivalry weakens the ability of the external well to attract protons in these two configurations. As a result, the increase in the nuclear charge radius as A increases in the lead isotope family is less pronounced for the g -conf and g^* -conf than for the i -conf. This clarifies why the i -conf exhibits a more pronounced kink than the g -conf (and g^* -conf) in lead isotopes.*

In Fig. 16, it can be seen that, for $l_a = 0$, the behaviour of $\langle r_a \rangle$ as a function of A for the g^* -conf approaches that of the i -conf. However, it approaches that of the g -conf as l_a increases. The behavior of $\langle r_a \rangle$ for $l_a = 0$ is partly fortuitous since $\delta V_{\text{cent}}(r, \epsilon)$ differs significantly between the i -conf and g^* -conf across the nuclear volume. Consequently, one would expect a different behaviour of $\langle r_a \rangle$ for any orbital in the i -conf and g^* -conf. However, the convergence of the behaviour of $\langle r_a \rangle$ for the g^* -conf and g -conf as l_a increases can be explained as follows. The density distribution corresponding to nodeless proton orbitals with small values of l_a is high in the inner part of the nucleus, where $\delta V_{\text{cent}}(r, \epsilon)$ differs significantly between the two configurations. Consequently, as it happens, different behaviour of $\langle r_a \rangle$ can be expected for these orbitals in the g -conf and g^* -conf. However, as the value of l_a for the proton orbital increases, the density distribution for this orbital becomes more significant at larger values of r , where $\delta V_{\text{cent}}(r, \epsilon)$ becomes very similar for the two configurations. Consequently, $\langle r_a \rangle$ behaves similarly in both the g -conf and g^* -conf.

3.2.4 The kink effect in relativistic models other than the standard RMFA

We have found that within the RMFA with the NL3* parameter set, the small components of the valence neutron orbitals in lead isotopes with $N > 208$ play an essential role in the generation of the kink. It would be interesting to know whether the role of these small components in other relativistic models is similar to the one found in our RMFA. We discuss this topic below.

The magnitude of the small component F_a of an orbital a is much smaller than that of the large component G_a (see Fig. 5), and its contribution to the nuclear density is much smaller than that of the G_a component. However, as explained in Subsec. 3.2, the contribution of the F_a component to the central potential $V_{\text{cent}}(r, \epsilon)$ in the Schrödinger-like equation (15) in our model has a factor approximately five times greater than that of the G_a component. (This factor is, roughly, the quotient $[\frac{g_\omega^2}{m_\omega^2} - \frac{g_\rho^2}{m_\rho^2} + \frac{g_\sigma^2}{m_\sigma^{*2}}]/[\frac{g_\omega^2}{m_\omega^2} - \frac{g_\rho^2}{m_\rho^2} - \frac{g_\sigma^2}{m_\sigma^{*2}}]$)

inside the nucleus, see Eq. (29) and Fig. 4). That is why its contribution becomes relevant in the potential $V_{\text{cent}}(r, \epsilon)$. This factor may change slightly from a specific parameter set to another in the RMFA, but it is not arbitrary. The saturation conditions of nuclear matter (saturation density, ρ_{B0} , energy per particle and symmetry energy at the nuclear density ρ_{B0} and compressibility modulus around ρ_{B0}) determine the model parameters and, consequently, the prior quotient and other model properties, such as, for example, the strength of the SO interaction.

Additional parameters may come into play for alternative realistic models that differ from the RMFA with the NL3* parameter set we have utilised, and the equations determining the saturation conditions may undergo modifications compared to ours. Nevertheless, the contribution of the small component of the Dirac spinors to the potential $V_{\text{cent}}(r, \epsilon)$ must still play an essential role for the saturation conditions to be met. Consequently, it can be expected that the small component of the valence neutron orbitals in the lead isotopes will continue to be essential in forming the kink for any nuclear relativistic model.

We have verified, in particular, that in the RMFA with the NL-Z parameter set [26], qualitatively similar results to those reported in this work for the NL3* parameter set are found. The minor differences can be attributed to the significantly distinct masses of the corresponding effective σ -mesons, leading to different ranges of the nucleon-nucleon attractive force due to the scalar field in the two sets.

4 Conclusions

Within the framework of the relativistic mean field approximation (RMFA), we have shown that the kink in the charge radii of lead isotopes is strongly related to the direct effects of the small component of the sp Dirac spinors of the valence neutrons on the central potential, $V_{\text{cent}}(r, \epsilon)$, in the Schrödinger-like equation equivalent to the Dirac equation. This is so, essentially, because the contributions to this potential from the σ -scalar and ω -vector fields, which depend directly on the scalar and nucleon densities, are very large and have opposite signs. These two facts combined greatly increase the contribution of the small component of the Dirac spinors, relative to that of the large component, to $V_{\text{cent}}(r, \epsilon)$. This allows that the small component of the valence neutron orbitals in lead isotopes with $N > 208$ plays an essential role in describing their nuclear charge radii according to experimental data. *The occupancy of these orbitals produces, through their small component, a repulsive potential in the inner part of the nucleus that favours the increase of the nuclear charge radius and, consequently, the kink formation.*

Our results within the RMFA indicate that the impact of the spin-orbit (SO) interaction on the kink through its influ-

ence on the wave functions of the valence neutrons is relatively minor in the case of the $1i$ orbitals, but it becomes significant for the $2g$ orbitals. Our results also reveal that relativistic effects, arising from the small component of the Dirac spinors, make the valence neutrons of a SO doublet more efficient for the generation of the kink when they occupy the orbital with $j = l - 1/2$ than when they occupy the orbital with $j = l + 1/2$. This is because the repulsive potential produced by the effect of the small component of those orbitals in the inner part of the nucleus, which favours the increase of the nuclear charge radius, is stronger and takes relevant values deeper within the nucleus for the orbital with $j = j_-$ than with $j = j_+$. This fact essentially explains why the former is more kinky than the latter, despite both having very similar radial big components and rms radii.

We have also found that the self-consistent or rearrangement indirect effects of the valence neutrons on lead isotopes induce significant changes in the proton central potential $V_{\text{cent}}(r, \epsilon)$ that notably favour the increase in the magnitude of the kink.

Although we have focused our study on the lead isotopic family, the ideas developed in this work can be applied to any other isotopic family. However, the model may not necessarily explain the observed behaviour of their nuclear charge radii.

The key to the success of the relativistic models in generating the experimentally observable kink effect in lead isotopes is the essential role that the small components of the sp Dirac spinors play in the sp central potential ($\simeq S(r) + V(r)$) of the Dirac and Schrödinger-like equations. Consequently, the conclusions reached in this work using the RMFA and the NL3* parameter set can be considered qualitatively valid, quite generally, for all usual relativistic models, and it can be stated that *the kink effect in relativistic models has an intrinsic relativistic origin*.

Acknowledgements The authors are grateful to N. Sandulescu for stimulating discussions and a referee, particularly, for his constructive criticism and valuable comments.

Funding Open Access funding provided thanks to the CRUE-CSIC agreement with Springer Nature.

Data availability This manuscript has no associated data or the data will not be deposited. [Authors' comment: There is no additional data besides those displayed in the figures.]

Open Access This article is licensed under a Creative Commons Attribution 4.0 International License, which permits use, sharing, adaptation, distribution and reproduction in any medium or format, as long as you give appropriate credit to the original author(s) and the source, provide a link to the Creative Commons licence, and indicate if changes were made. The images or other third party material in this article are included in the article's Creative Commons licence, unless indicated otherwise in a credit line to the material. If material is not included in the article's Creative Commons licence and your intended use is not permitted by statutory regulation or exceeds the permit-

ted use, you will need to obtain permission directly from the copyright holder. To view a copy of this licence, visit <http://creativecommons.org/licenses/by/4.0/>.

References

1. P. Campbell, I. Moore, M. Pearson, *Prog. Par. Nucl. Phys.* **86**, 127 (2016)
2. M.M. Sharma, G.A. Lalazissis, P. Ring, *Phys. Lett. B* **317**, 9 (1993)
3. S. Marcos, L.N. Savushkin, M. López-Quelle, R. Niembro, P. Bernardos, *Phys. Lett. B* **507**, 135 (2001)
4. R. Niembro, S. Marcos, M. López-Quelle, L.N. Savushkin, *Phys. At. Nucl.* **75**, 269 (2012)
5. S.E. Agbemava, A.V. Afanasjev, D. Ray, P. Ring, *Phys. Rev. C* **89**, 054320 (2014)
6. U.C. Perera, A.V. Afanasjev, P. Ring, *Phys. Rev. C* **104**, 064313 (2021)
7. T. Naito, T. Oishi, H. Sagawa, Z. Wang, *Phys. Rev. C* **107**, 054307 (2023)
8. N. Tajima, P. Bonche, H. Flocard, P.-H. Heenen, M.S. Weiss, *Nucl. Phys. A* **551**, 434 (1993)
9. H. Nakada, *Phys. Rev. C* **100**, 044310 (2019)
10. P.-G. Reinhard, H. Flocard, *Nucl. Phys. A* **584**, 467 (1995)
11. M. Goddard, P.D. Stevenson, A. Rios, *PRL* **110**, 032503 (2013)
12. H. Nakada, T. Inakura, *Phys. Rev. C* **91**, 021302(R) (2015)
13. M.M. Sharma, G.A. Lalazissis, J. König, P. Ring, *Phys. Rev. Lett.* **74**, 3744 (1995)
14. S.A. Fayans, S.V. tolokonnikov, E.L. Trykov, D. Zawischa, *Phys. Lett. B* **338**, 1 (1994)
15. S.A. Fayans, D. Zawischa, *Phys. Lett. B* **383**, 19 (1996)
16. S.A. Fayans, S.V. tolokonnikov, E.L. Trykov, D. Zawischa, *Nucl. Phys. A* **676**, 49 (2000)
17. P.-G. Reinhard, W. Nazarewicz, *Phys. Rev. C* **95**, 064328 (2017)
18. H. Nakada, *Phys. Rev. C* **92**, 044307 (2015)
19. W. Horiuchi, T. Inakura, *Phys. Rev. C* **105**, 044303 (2022)
20. S. Marcos, R. Niembro, M. López-Quelle, *EPJ Web of Conferences* **290**, 02026 (2023)
21. T. Day Goodacre *et al.*, *Phys. Rev. Lett.* **126**, 032502 (2021)
22. T. Day Goodacre *et al.*, *Phys. Rev. C* **104**, 054322 (2021)
23. U.C. Perera, A.V. Afanasjev, *Phys. Rev. C* **107**, 064321 (2023)
24. J. Boguta, A.R. Bodmer, *Nucl. Phys. A* **292**, 413 (1977)
25. A. Bouyssy, S. Marcos, and Pham Van Thieu, *Nucl. Phys. A* **424**, 541 (1984)
26. M. Rufa, P.-G. Reinhard, J.A. Maruhn, W. Greiner, M.R. Strayer, *Phys. Rev. C* **38**, 390 (1988)
27. P. Ring, *Prog. Part. Nucl. Phys.* **37**, 193 (1996)
28. G.A. Lalazissis, S. Karatzikos, R. Fossion, D. Pena Arteaga, A.V. Afanasjev, P. Ring, *Phys. Lett. B* **671**, 36 (2009)
29. A. Bouyssy, J.F. Mathiot, Nguyen Van Giai, S. Marcos, *Phys. Rev. C* **36**, 380 (1987)
30. R. Brockmann, *Phys. Rev. C* **18**, 1510 (1978)
31. L.N. Savushkin, H. Toki, *The Atomic Nucleus as a Relativistic System* (Springer, Berlin, 2004)
32. J.J. Sakurai, *Advanced Quantum Mechanics* (Addison-Wesley, New York, 1967)
33. Y. Nedjadi, J.R. Rook, *Nucl. Phys. A* **484**, 525 (1988)
34. V.I. Isakov, *Phys. Part. Nucl.* **38**, 269 (2007)
35. P. Ring, P. Schuck, *The Nuclear Many-Body Problem* (Springer, Berlin, 1980)
36. I. Angeli, *At. Data Nucl. Data Tables* **87**, 185 (2004)
37. J.N. Ginocchio, *Phys. Rev. Lett.* **78**, 436 (1997)
38. J.N. Ginocchio, D.G. Madland, *Phys. Rev. C* **57**, 1167 (1998)
39. S. Marcos, M. López-Quelle, R. Niembro, L.N. Savushkin, *Eur. Phys. J. A.* **20**, 443 (2004); **37**, 251 (2008)